Microstructure evolution and grain growth characteristics of laser surface melted Inconel 625

By Liangyi Sun (20615471)

Submitted in partial fulfillment of the conditions for the award of the Master's degree

Supervised by Dr. Hao Chen

Department of Mechanical, Materials, and Manufacturing Engineering, Faculty of Science and Engineering,
University of Nottingham Ningbo China

Preface

This thesis is submitted for the degree of Master of Research at the University of Nottingham Ningbo China. The research work was carried out under the supervision of Professor Hao Chen and Dr. Adam Rushworth in the Faculty of Science and Engineering.

It is certified that the work presented in this thesis is original, and suitable references are made to any work cited from the literature.

The list of publications from the work presented in this thesis is presented here:

- H. Chen, **L. Sun**, L. Li, W. Zhu, Q. Gong, R.D. Castro, A. Rushworth, Microstructure evolution and grain growth characteristics of IN625 in laser surface melting: Effects of laser power and scanning speed, Journal of Materials Processing Technology 331 (2024) 118525. https://doi.org/10.1016/j.jmatprotec.2024.118525

Acknowledgements

This dissertation represents a significant milestone in my long and challenging learning journey, and I am deeply grateful for the support of numerous individuals during this period. My deepest gratitude goes first and foremost to Dr. Hao Chen for his consistent and valuable guidance throughout my Master's degree. He has walked through all the stages of the writing of this thesis. Without his consistent and illuminating instruction, this thesis could not have reached its present form. His advice has not only guided my research but has also deepened my understanding of the scientific problem. I am fortunate to have benefited from his vast knowledge and exceptional qualities of patience and support.

I also express my gratitude to Dr. Lingshan Li for his encouraging discussions that provided me with a multifaceted perspective on this project. Additionally, he has offered direction and inspiration for further research and exposed me to research methods in other related fields that have profoundly influenced my future development. I am also thankful for the collaborative efforts of my colleague Yusheng Zong.

I am deeply grateful to my beloved family for their loving consideration and great confidence, for their unwavering motivation, patience, and care during my education and life journey. Their support has been instrumental in completing this dissertation. Finally, I would like to thank all the individuals who have supported me, and I wish them happiness and success in their endeavours.

Abstract

Inconel 625 is a Ni-based superalloy widely used in nuclear and aerospace applications because of its high strength and corrosion resistance. The current thesis investigated the effects of laser power and scanning speed on the microstructure evolution and grain growth characteristics of IN625 in laser surface melting. Laser powers of 400 W, 600 W, and 800 W at scanning speeds from 200 mm/min to 800 mm/min were employed to melt the surface of as-cast IN625 using a continuous Yb-doped fibre laser. The microstructure from the surface to the melt pool boundary was characterized by scanning electron microscopy (SEM) and electron backscattered diffraction (EBSD). It was shown that a cellular structure was developed at low energy densities ($\leq$ 240 J/mm^2), due to that low energy densities resulted in more rapid solidification. A coarse grain region was found near the surface after melting, and a columnar grain growth region was formed close to the melt pool boundary at increasing laser power. Large-angle grain boundaries were eliminated, and medium-angle grain boundaries exhibited an area fraction of 90% after laser surface melting. This was because the twinned grains were fully melted in the melt pool, and no twins were formed after solidification. An analytical approach was proposed to estimate the melt pool depth, and good agreement between experimental and calculated melt pool depth was obtained at a laser power of 400 W and 600 W. In addition, a surface hardening effect was noticed at high scanning speeds, which was likely due to the heavy element segregation and secondary phase formation during laser surface remelting.

Contents

List of Figures

List of Tables

Abbreviations

AD   As-deposited

AED   Area energy density

AR   As-received

BSE   Backscattered electron

EBSD   Electron backscattered diffraction

EDM   Electron discharge machining

EDS   Energy dispersive X-ray spectroscopy

FVM   Finite volume method

HCS   Heat conduction equation

IN625   Inconel 625

IPF   Inversed pole figure

LSM   Laser surface melting

MPW   Melt pool width

MPD   Melt pool depth

SLM   Selective laser melting

SEM   Scanning electron microscopy

Chapter 1 Introduction

1.1 Background

In recent decades, laser technology has been widely employed in machining, welding, additive manufacturing and surface treatment, due to its high energy density and good dimensional accuracy and precision [1-3]. To enhance the surface properties, laser surface treatment is of great interest for modifying microstructures and reducing surface defects. Among the available laser surface treatment methods, laser surface melting (LSM) exhibits a promising approach to controlling the surface microstructure by utilizing a laser beam to selectively melt the surface.

An optimized set of laser parameters should be applied to get desired properties depending upon applications. Given the appropriate processing parameters during laser surface melting, sufficient heat input is provided to heat the surface of the material above its melting temperature, forming a melt pool near the surface, which is then rapidly cooled and solidified. The rapid heating and cooling cycles often result in significant changes in the microstructure and grain characteristics when compared to the bulk material. The heat input into the material is mainly dominated by two factors, namely the laser power and scanning speed. The choice of laser power is critical to achieve sufficient melting of the surface. It is understood that a low laser power (e.g. < 200 W) will cause insufficient melting, whilst too high a laser power (> 1000 W) will lead to over-melting and excessive thermal stress. Meanwhile, the cooling behaviour during laser surface melting is also strongly influenced by the laser scanning speed [4]. It has been reported that excessive heat accumulation occurs when the scanning speed

is too slow at an adequate laser power [5], which often generates micro-pores and shrinkage cavities, while very fast scanning speed may produce a low energy density and insufficient melting [6]. Thus, careful control of the laser power and scanning speed is essential to obtain desirable microstructure and surface properties.

Studies have shown that the grain size in alloy can be significantly altered through LSM, with laser power and scanning speed being critical parameters. As the laser power increases, a coarse grain region appears near the surface, and a columnar grain growth region forms close to the melt pool boundary, suggesting that higher energy inputs can lead to grain growth [7].

These above studies have demonstrated that the variations in laser power and scanning speed have a strong influence on the resultant microstructure and grain growth behaviour during laser surface melting. However, work concerned with the grain boundary evolution in the melt zone during laser surface melting, especially the grain boundary angle changes, appears quite sparse, due to the complex interaction between laser power and scanning speed. It is crucial to elucidate the effects of these parameters on the microstructure evolution and grain growth characteristics, in order to achieve better microstructure control and process optimisation.

1.2   Aims and objectives

This study aims to investigate the microstructure evolution and grain growth characteristics at different laser power and scanning speeds in laser surface melting. In particular, the formation of cellular structures under various combinations of laser power and scanning speed is studied and the subsequent grain growth mechanism is

detailed. As-cast IN625 is used as a reference material to illuminate the microstructure changes after laser surface melting. A continuous laser at powers of 400 W, 600 W, 800 W and scanning speeds ranging from 200 mm/min to 800 mm/min was employed to melt the surface of as-cast IN625. The microstructure and grain growth characteristics were analysed by scanning electron microscopy (SEM) and electron backscattered diffraction (EBSD). The combined effects of laser power and scanning speeds on the microstructure evolution and grain growth behaviour are discussed. An analytical model is developed to evaluate the temperature distribution across the melt pool, in an attempt to reveal the evolution of melt pool depth under various laser power and scanning speed conditions.

1.3 Contributions and overview

This thesis is organised around several chapters presenting an investigation on the microstructure evolution and grain growth characteristics of IN625 during laser surface melting. The main chapters of this thesis are listed below:

Chapter 1 introduces the background of LSM and identifies the aims and objectives of this thesis.

Chapter 2 is a literature review section, which introduces the technique of laser surface melting, the morphology of the molten pool and the grain changes after melting, and the related mathematical modelling.

Chapter 3 describes in detail the selection of the experimental samples, the choice of the laser parameters (e.g. laser power and scanning speed) and the laser scanning

strategy. The sample observation positions as well as what related characterisation techniques were included.

Chapter 4 focuses on a detailed description of the microstructural evolution and grain growth characteristics in laser surface melting at different laser powers and scanning speeds.

Chapter 5 summarises the main findings of this thesis.

Chapter 6 discusses some limitations of this work and suggests future research directions.

Chapter 2 Literature review

2.1   Laser surface melting

Laser surface melting is a post-treatment process of melting the top thin layer of material with the introduction of the laser [8]. This technique is a heat treatment technique that modifies surface microstructure and improves mechanical properties like fatigue strength, wear resistance, and corrosion resistance ultimately enhancing performance [5, 9]. LSM is preferable as compared to other techniques because it is accurate and efficient. It has the advantage of treating selective surfaces only [10], which is unique to improving its properties and performance instead of treating whole material (as done in other heat treatment processes). Generally, there are five major types of lasers i.e. gas lasers, solid-state lasers, fiber lasers, liquid lasers, and semiconductor lasers [11]. Commonly used sub-types of lasers in the remelting process are CO_2 laser, Nd: YAG laser, fiber laser, High Power Diode Laser (HPDL), and excimer laser. Nd: YAG lasers can operate in both continuous wave and pulsed modes, providing flexibility for different types of applications [1]. It is available in a wide range of power levels and is suitable for processing both small and large parts [12]. The depth of melting can be controlled by adjusting the laser parameters, allowing the surface layer to be modified without significantly affecting the bulk material [13]. Wavelength has an inverse relation with absorptivity, usually, the CO_2 laser has a wavelength of 10.6 μm while Nd: YAG has a wavelength of 1.064 μm [10], Nd: YAG laser's wavelength can be highly absorbed by most metals [1]. In summary, Nd: YAG

lasers are often chosen for LSM, as they are able to control the melting process at the microstructural level, thus improving material properties. There are three basic modes of lasers, i.e. continuous wave laser, pulsed laser, and ultra-high speed laser. A diagram of a continuous laser surface melting device is shown in **Fig. 2.1** [7].
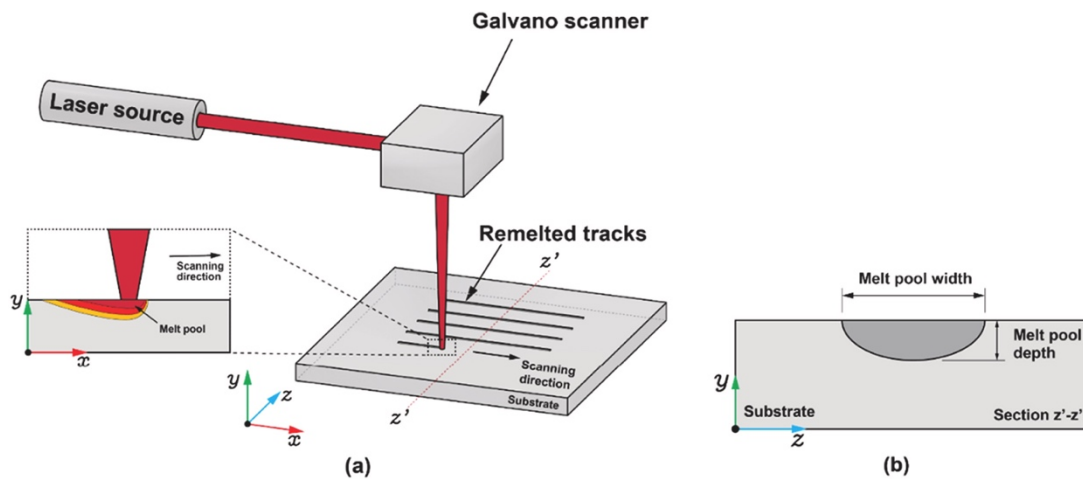
Fig. 2.1 Schematic diagram of the experimental set-up for laser surface melting [7].

In laser surface melting, the relevant parameters are very important. General laser processing parameters are laser power, laser energy, energy density, scanning velocity, exposure time, point distance, beam diameter, beam overlapping, pulse duration, hatch spacing, spot size, and layer thickness, but the most influential parameters are laser power, scanning velocity and energy density [14-20]. In order to achieve good mechanical properties by laser surface melting, an optimized set of laser processing parameters is essential. Optimized laser parameters applied to a material will change its properties, such as increasing the hardness of the material and improving corrosion resistance, etc. (e.g. **Fig. 2.2**).

Fig. 2.2 Effect of optimised machining parameters on material properties.

2.2 Process parameters of LSM

Shoja-Razavi [21] worked on laser power and scanning velocity to optimize LSM parameters for Stellite 6 coating on 316L alloy deposited by High-Velocity Oxygen Fuel (HVOF). This research provided contradictory results as microhardness was decreased by 17% after treating coated steel disks with Nd: YAG laser at varying laser power ranging from 100 W to 350 W and scanning velocity ranging from 4 mm/s to 6 mm/s. However, an 86% reduction in porosity was observed at an optimized set of 200 W power and 4mm/s scanning velocity. LSM of Stellite coating can refine the microstructure and improve its characteristics under good parameters [22]. Ciubotariu et al. [23, 24] reported that 1550 W is the optimum pulse power of Nd: YAG laser for complete melting and proper bonding of HVOF thermally sprayed stellite 6 coating to base stainless steel alloy. Chen et al. [25] studied the impact of laser scanning speeds of 314 steel after LSM through a nanosecond pulsed laser. They demonstrated that microhardness increases with an increase in scanning velocity. Vidyasagar et al. [26].also manipulated laser power and pulse frequency of LSM to find an optimized set

for better corrosion resistance of Nickel-Titanium alloy, also known as Nitinol. 2 mm thick, 200 mm long, and 200 mm wide sheet of nitinol was prepared. Samples of 10 mm × 10 mm were cut from this sheet and were subjected to a nanosecond pulsed fiber laser at a varying laser power of 5 W to 45 W and pulse frequency of 50 kHz to 250 kHz. After the treatment, corrosion testing was performed on each sample. The optimum parameters were 33 W power and 177 kHz frequency which provided better corrosion resistance [26]. Along with laser power, Ghorbani et al. [17] varied layer thickness, point distance, and exposure time of LSM while working on inclined 316L stainless steel parts processed by LSM. Those inclined parts were subjected to a Ytterbium fiber laser at different layer thicknesses, point distances, exposure times, and laser power (as shown in **Table 2.1 [17]**). After LSM, surface roughness was measured using Marsurf M300-C machine. Results showed that very high exposure time and power can lead to uneven remelted zone whereas very low exposure time and power do not affect the microstructure considerably. The optimized set of parameters was investigated using simulation on Minitab software. Those parameters were 141.41 μm of layer thickness, a point distance of 47.77 μm, an exposure time of 400 μs, and a power of 169.19 W. At the optimized parameters, the surface roughness of Yp = 0.54 was recorded.

Table 2.1 Variation in parameters during LSM of 316L [17].

Dependent Variables	Parameter 1	Parameter 2
Shell layer thickness (μm)	100	150
Point distance (μm)	30	50
Exposure time (μs)	200	300
Laser power (W)	150	175

Laser energy density is another important laser processing parameter. The effect of laser energy density during LSM on H13 steel was explored to find the optimum energy density for improved structure and properties. Annealed steel plates with dimensions $30 \times 100 \times 15$ mm^3 were subjected to fiber laser at manipulated laser power, scanning velocity, and laser energy density (as shown in **Table 2.2 [27]**).

Table 2.2 Manipulated parameters during LSM of H13 steel [27].

Sample number	Laser power	Energy density	Scanning velocity
1	1650 W	110 J/mm^2	3 mm/s
2	1800 W	120 J/mm^2	3 mm/s
3	1800 W	90 J/mm^2	4 mm/s

Results indicated an increase in coarse grains with an increase in energy density. However, residual tensile stresses were converted into residual compressive stresses at 120 J/mm^{2}which is good for enhanced fatigue behavior [27]. During LSM, lower laser power and higher scanning velocity were more energy efficient in the Z-direction of the melt bed whereas higher power and lower scanning speed were more energy efficient in the Y-direction of the melt bed [28]. Zhang et al. reported that during LSM of Mg-9%Al powder mixture lowest porosity was obtained at 15 W laser power, and 0.02 m/s scanning velocity whereas the highest hardness was obtained at 15 W power and 0.04 m/s scanning velocity [29]. LSM can enhance mechanical properties but only in optimized parametric conditions. Optimized laser power and scanning velocity can enhance the microstructure and hardness of materials whereas an optimized set of power and pulse frequency can enhance corrosion resistance and hardness. Too much

exposure time and power can cause uneven melting. Increasing energy density results in coarser grains but an increase in residual compressive stresses.

In summary, laser power, scanning velocity and energy density are some parameters that have the most influence on the properties of materials. The microstructure of materials is mainly influenced by laser power and scanning velocity. Proper laser power and scanning speed can improve material microstructure and increase hardness (as shown in **Fig. 2.3 [1]**)
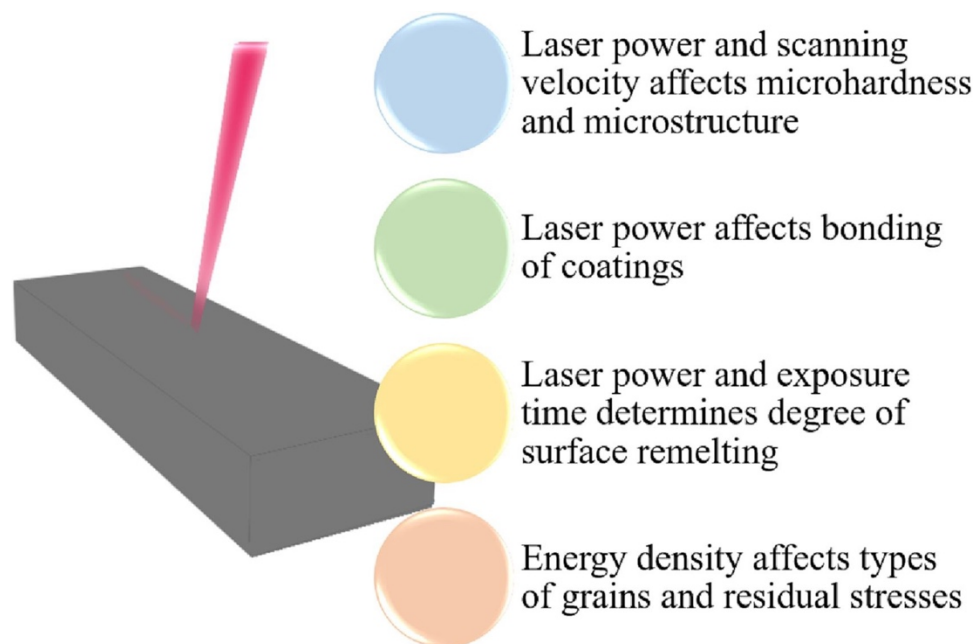
Fig. 2.3 The influence of different laser processing parameters on materials' properties [1].

2.3 Microstructural evolution and property changes

The properties of alloy undergoes significant evolution during the laser surface melting process. These property changes are closely related to the laser process parameters, such as laser power, scanning speed and scanning strategy. Hitherto, work concerned with the effects of laser power and scanning speed on the microstructure evolution and mechanical/chemical properties during laser surface melting have been reported. Yasa

et al. [30] investigated the effects of laser surface melting on the surface quality of laser additively manufactured parts using different laser powers and scanning speeds. This is due to the creation of larger and deeper melt pool with increase in energy density. A significant improvement in surface roughness was reported when using a medium laser power at a relatively low scanning speed. Praharaj et al. studied the surface hardness and wear properties of IN625 using a 250 W fibre laser as the heat source in laser surface melting [31]. They analysed the as-deposited (AD) and remelted (RM) samples using a stereo microscope and the images of the samples are shown in **Fig. 2.4** [31] to investigate the effect of laser melting on the surface morphology. It was observed that the surface of AD sample consists of partially melted powder particles in **Fig. 2.4**a. This could be due to less energy density (low laser power or high scanning speed) or larger powder particle size. During the deposition process, the laser source produced a molten pool on the surface in **Fig. 2.4**b - **Fig. 2.4**f, the melted layer has a regular corrugated shape. The melt pool has an inhomogeneous surface tension due to the presence of different combinations of elements with different volume percentages [32]. During the initial stage of solidification process, the kinetic energy of the laser beam was converted into the surface energy of the molten metal resulting in formation of smaller metal droplets. Each metal droplet strives for the lowest possible surface energy under the influence of both surface tension and gravity force inside the melt pool. As a consequence, a small quantity of the metal droplets splashed from the molten pool and later solidified as spherical balls on the already deposited surface [33].
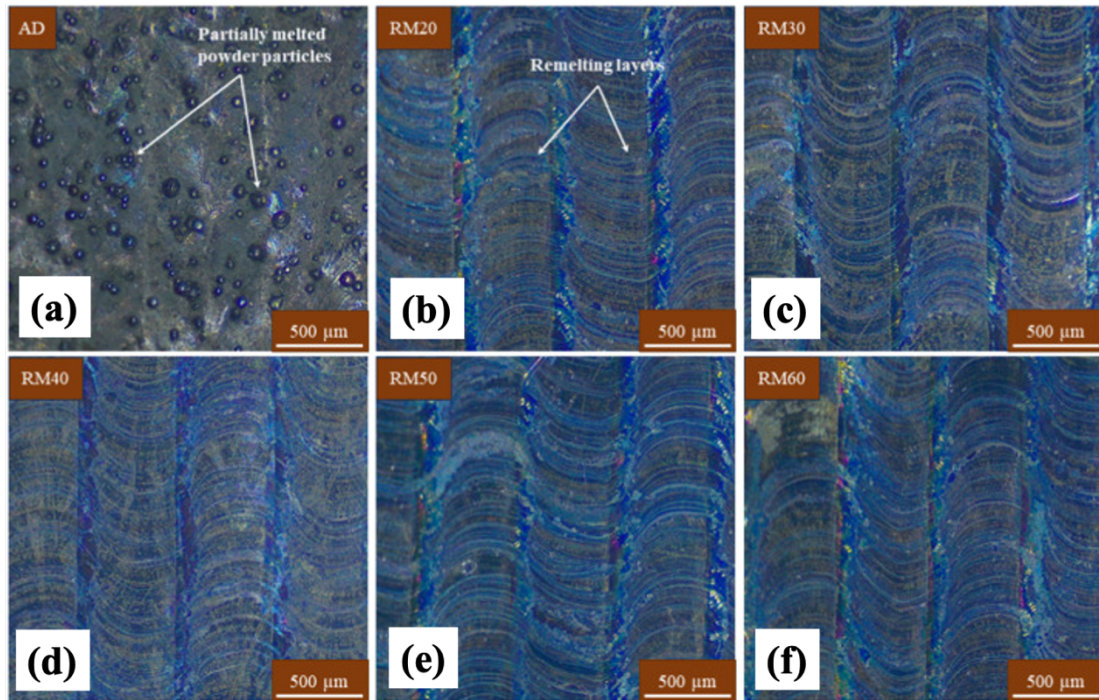
Fig. 2.4 Stereomicroscopic images of IN625 samples in AD condition (with presence of partially melted powders) and RM conditions (for different energy densities) [31].

Apart from this, the formation of these metal droplets could be due to the non-wettability of the molten metal with the solidified surface. This mechanism was reported by Das et al. [34]. The surface quality of the AD sample was greatly influenced by the presence of partially melted powder particles. After melting, the partially melted powder particles were melted completely by receiving the energy from the laser source. The repeated melting and solidification of the molten material filled the valleys present on the surface of the AD sample. Hence, the LSM resulted in a comparatively smoother surface than the AD condition. The surface roughness of all the samples was determined using a 3D optical profilometer to show a relative comparison of surface quality among the AD and RM samples. The 3D surface morphology value of the samples is displayed in **Fig. 2.5** [35]. It was found that the surface morphology decreases significantly after

laser melting. The 3D surface morphology of the AD sample also confirmed the presence of partially melted powder particles.
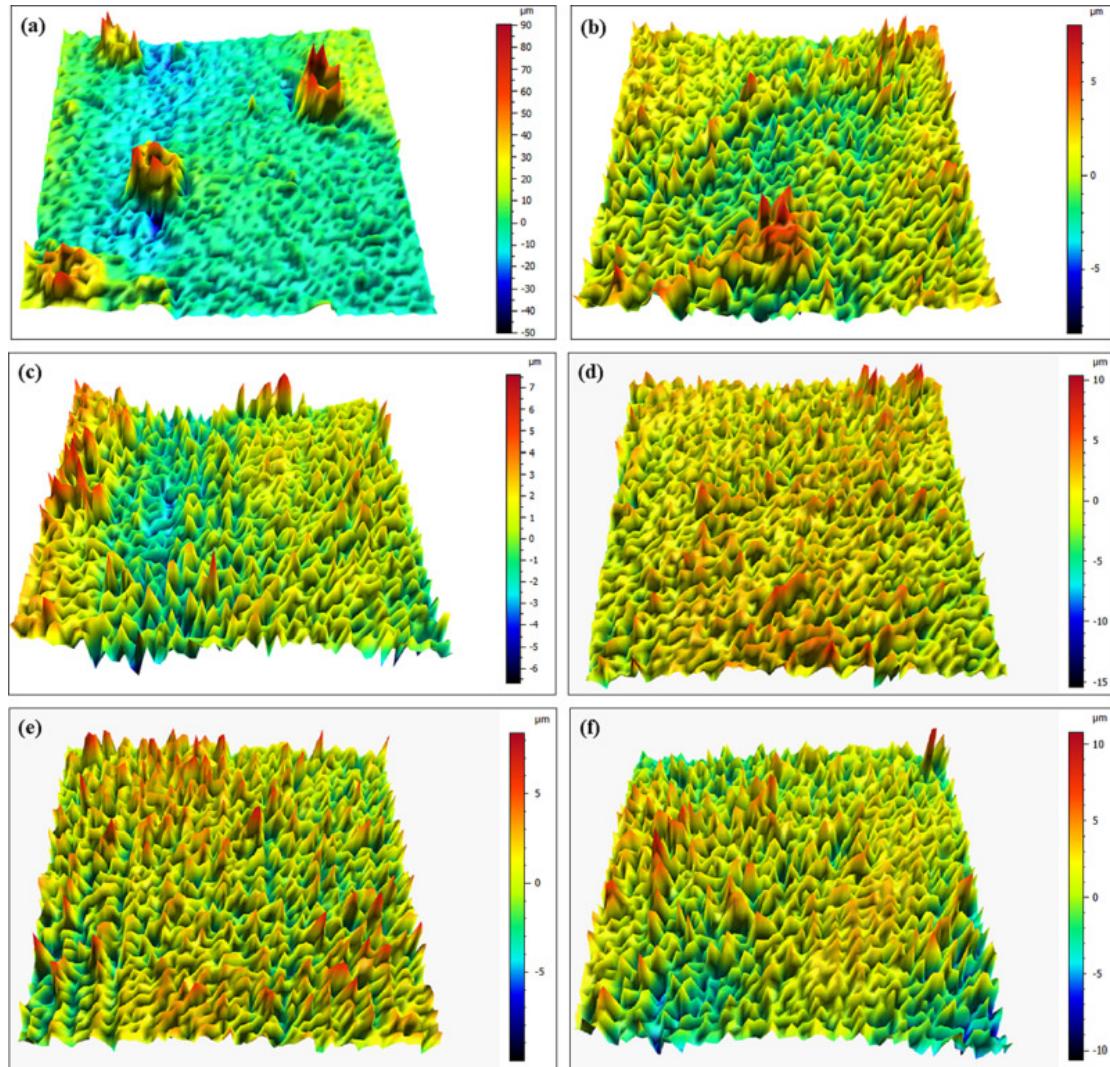
Fig. 2.5 3D surface morphology of the samples obtained using profilometer before wear test (a) AD, (b) RM20, (c) RM30, (d) RM40, (e) RM50, (f) RM60 [35].

The surface roughness value (S_a) for all the samples is plotted in **Fig. 2.6**(a) [35]. The S_a value was determined by area scanning (250 μm × 250 μm) of the samples at 5 different locations. The S_a value obtained for the AD sample was 13.51 μm. It can be noted that S_a decreases significantly after melting when compared to the AD sample. The least value of S_a after melting was 2.19 μm which was obtained for RM20 sample

(melted track with the highest scanning speed and lowest linear energy density). This is because, the lowest linear energy density (20 J/mm) used in this study is sufficient to melt the partially melted particles present on the surface and thereby improve the surface quality. Further, a small increase in S_a value was observed with increase in linear energy density (decrease in scanning speed) as shown in **Fig. 2.6**b [35]. This is due to the creation of larger and deeper melt pool with increase in energy density. It was found that the wear properties were greatly improved due to solid solution strengthening and microstructure refinement. Wang et al [36]. examined the surface roughness under different melting times and reported that the roughness decreased with melting time.
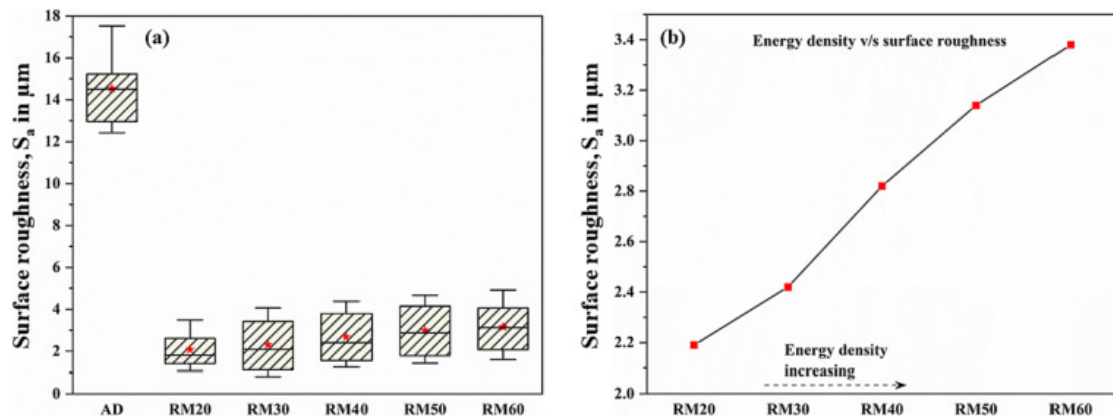
Fig. 2.6 Comparison of Surface roughness (obtained from full area scan) among the AD and RM surfaces before wear test (a), the effect of energy density on surface roughness for RM samples (b) [35].

The microstructure of the alloy also changes significantly after laser surface melting. Vaithilingam et al. [37] reported that the surface chemical composition and oxidation behaviour were affected by the microstructure changes after laser surface melting. More specifically, It was further reported by Anishetty et al. that the coarsening of microstructure and increase of segregation occurred and a refinement of microstructure

with cellular grains was observed [38] when the scanning speed increased. A detailed electron backscattered diffraction (EBSD) analysis was conducted to confirm the distribution of different phases and their orientation mapping. **Fig. 2.7** [38] presents the EBSD phase mapping of (a) as-received Ti-13Nb-13Zr and the same after laser composite surfacing with (b) 1000 W applied power, 10 mm/s scan speed, (b) 1000 W applied power, 20 mm/s scan speed and (c) 1400 W applied power, 20 mm/s scan speed. The phase mapping in **Fig. 2.7**a [38] clearly reveals the presence of β phases (28.8%) and α/α' phases (71.2%) of acicular morphology. Similar phase distribution in Ti-13Nb-13Zr was also reported by [39]. **Fig. 2.7**b-**Fig. 2.7**d [38] shows the presence of dendritic carbides (TiC) dispersed in grain refined β and α/α' matrix. A comparison of **Fig. 2.7**b [38] with **Fig. 2.7**c shows that with increase in scanning speed, there is refinement of dendritic carbides, the increased area fraction of dendritic carbides and the presence of grain refined α/α' and β phases in the microstructure. On the other hand, a comparison between **Fig. 2.7**c and **Fig. 2.7**d [38] show that with increase in applied power, there is decreased area fraction of dendritic carbides and increased area fraction of β phase. A comparison of **Fig. 2.7**a with **Fig. 2.7**b- **Fig. 2.7**d [38], it may further be noted that due to composite surfacing, there is decreased area fraction of α/α' phase as compared to the as-received substrate. The decreased area fraction of α/α' phase due to composite surfacing is possibly attributed to rapid quenching and, hence, retention of β phase due to the availability of less time for the β to α/α' transformation. These studies have demonstrated that laser surface melting is able to modify the surface microstructure and

15

achieve desirable properties, given that the processing parameters are carefully controlled.
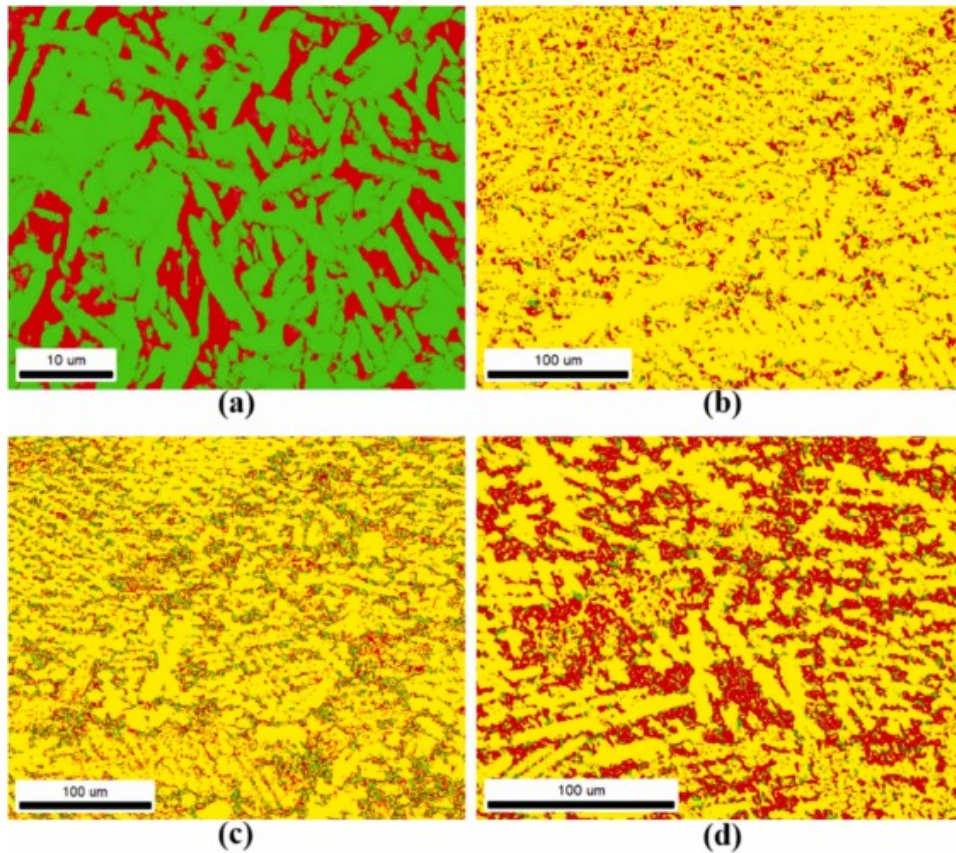
Fig. 2.7 EBSD phase mapping of (a) as-received Ti-13Nb-13Zr and the same after laser composite surfacing with (b) 1000 W applied power, 10 mm/s scan speed, (c) 1000 W applied power, 20 mm/s scan speed and (d) 1400 W applied power, 20 mm/s scan speed. Here, red colour indicates β phase, green colour indicates α/α' phase and yellow colour indicates the dendritic carbides [38].

2.4 Characteristics of grain structure

In addition to the microstructure and property modifications during laser surface melting, the grain structure characteristics also undergo a profound change from the surface to the bulk material [40]. Sun et al. [41] found that the surface microstructural feature of the AR and LSM specimens are also examined by EBSD, as shown in **Fig. 2.8**a and **Fig. 2.8**b [41]. The grains in the LSM specimen are indeed refined. The corresponding grain size distribution histograms exhibited in **Fig. 2.8**f and **Fig. 2.8**g

[41] indicate that the average size of the AR and LSM specimens are $\sim 36.7 \pm 3.8$ μm and 2.8 ± 0.8 μm, respectively. Since melting and solidification occur within a very short period of time and are limited to the top surface, the underlying matrix acts as an infinite heat sink without any appreciable change in microstructure. In the meantime, the large temperature gradient across the boundary between the melted surface and underlying substrate leads to a rapid cooling rate, and the grains of the molten layer do not have time to grow, resulting in refinement. They found that the large temperature gradient across the melt pool boundary led to a rapid cooling rate and grain refinement occurred due to insufficient time for the grains to grow in the melt zone.
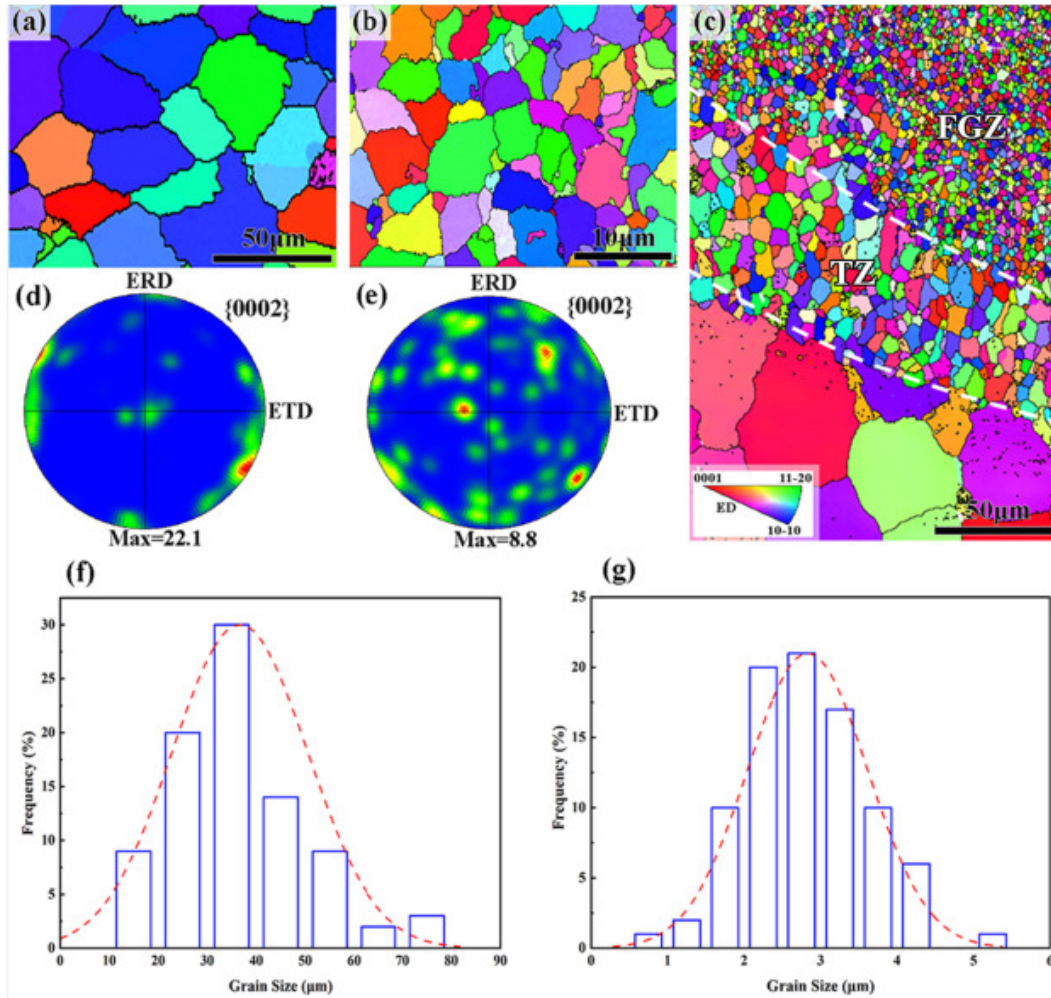
Fig. 2.8 EBSD results of AR and LSM specimens: (a) inverse pole figure maps of the surface of AR specimen. (b, c) the surface and the cross section of LSM specimen, respectively. The fine grain zone and transition zone are marked by fine grain zone (FGZ) and transition zone (TZ), respectively. (d, e) The {0002} pole figure maps corresponding to the regions shown in a and b, respectively. (f, g) The distribution histograms of the surface grain size of AR and LSM specimens, respectively [41].

Chong et al. further reported that preferred grain orientation can be developed during laser surface melting process [42]. **Fig. 2.9**a and **Fig. 2.9**b [42]shows the inverse pole figure (IPF) maps for the high-speed laser cladding (HLC) and laser surface melting coatings. It was clearly discovered that the grains of the HLC coating display random orientations (**Fig. 2.9**a [42]) and the (101) orientation was clearer in the liquid phase separation (LPS) zones. However, the (001) orientation was a preferential grain

orientation in the LSM coating. **Fig. 2.9**c and **Fig. 2.9**d [42] depicts the {111}, {011}, and {001} pole figures (PFs) of the HLC and LSM coatings, which indicate distributions of the pole density of the B2/BCC phase mixture along the build direction [43]. It could be seen that a more complex hybrid texture was formed in the LSM coating. The maximum texture index of each sample appeared at {001}. It indicated that {001} was the strongest dominant growth texture compared with {111} and {011}. The maximum texture index value of {001} was 2.32 and 1.57 in the HLC and LSM coatings, and the average texture index value of {001} was larger in the LSM coating. **Fig. 2.9**e and **Fig. 2.9**f [42] show the IPF of the HLC and LSM coatings. The LSM coating had an obvious preferred orientation in <001> crystallographic direction of polar density projection in the X-axis direction, and the other orientations were weakened. This was because LSM has an effect on the form of the melt pool, and the epitaxial growth of the grains was perpendicular to its boundary. Therefore, the LSM had a noticeable influence on the preferred orientation of grains and ultimately caused an anisotropy of the HLC coatings.
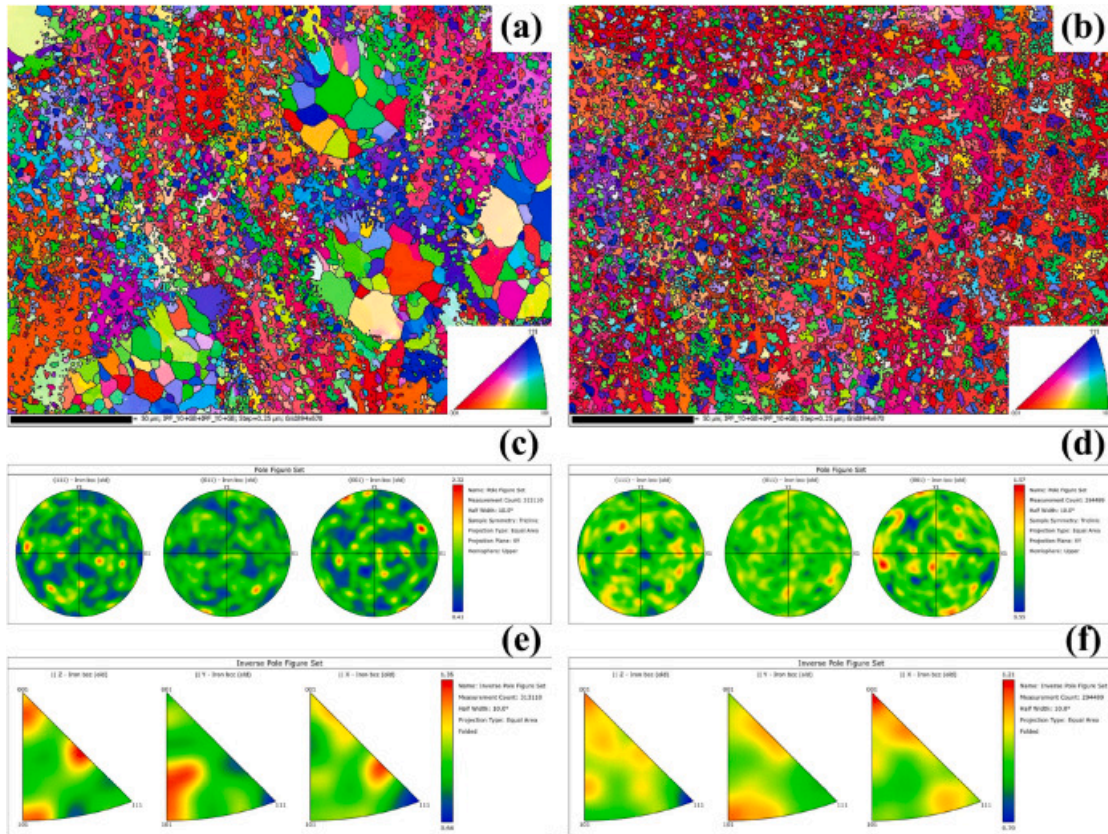
Fig. 2.9 EBSD analysis of the coatings prepared by HLC and reprocessed by LSM: (a) and (b) IPF maps, (c) and (d) pole figures (PF), and (e) and (f) IPFs [42].

However, the grain refinement and growth behaviour is strongly dependent on the combination of laser power and scanning speed. With the increase of melt pool depth at various laser parameters, grain growth across the melt pool also occurs and some coarse and columnar grains instead of refined grains can form. Yuan et al. [44] reported a typical directional columnar microstructure near the melt pool boundary after laser surface melting. As shown in **Fig. 2.10** [44], the LSM-treated sample is a typical oriented columnar microstructure with an average size of ~25 μm, as shown in the inset statistical graph. The columnar grains were found to grow epitaxially from the melt pool boundary towards the laser surface melted zone [45].
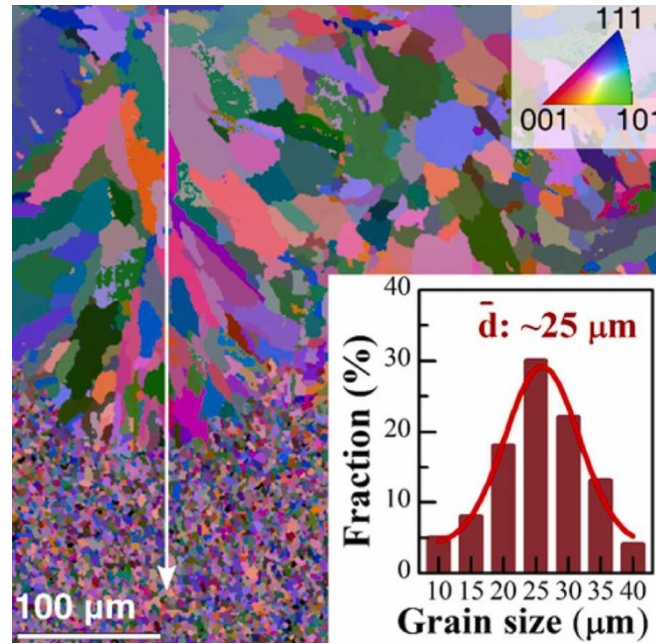
Fig. 2.10 Typical EBSD view of the cross-sectional plane of the 130 W laser melted sample with grain size distribution in the melted layer [44].

2.5   Numerical methods to analyse melt pool

Laser surface melting modified the microstructure and properties of treated material due to melting and intensive mixing of liquid material. The high heating and cooling rates were the reason for fine-grained microstructure. The microstructural changes in the treated material strongly depended on the type of material, its chemical composition and physical properties as well as the laser heat treatment parameters used. It was obvious, that laser melted zone could be formed only if the temperature at the surface was higher than melting point of treated material. Whereas, the formation of heat-affected zone was resulted from the laser heat treatment of substrate material. The knowledge about the temperature distribution across the axis of the laser track could be an important implement in the prediction of depth of melted zone and heat-affected zone. The evaluation of this temperature distribution is important for optimising laser processing parameters and improving processing efficiency and quality. At different

21

laser powers and scanning speeds, the temperature distribution will show different characteristics, which requires an effective analysis method to predict and control.

As early as the 1940s, Rosenthal [46] proposed an analytical method for estimating the temperature distribution during welding. This method describes the transfer of heat through the material by means of a mathematical model, which predicts the shape and depth of the molten pool. Rosenthal laid the foundation for subsequent research, and his models have shown good applicability and similarity in the field of laser surface melting. Building on Rosenthal's work, Ashby and Esterling further developed these semi-quantitative solutions. They have made it possible to more accurately approximate the heat flow after laser surface treatment by improving the model. These improvements include consideration of the complexity of the laser beam-material interaction, as well as the effect of the thermophysical properties of the material on the temperature distribution. Their work not only improved the prediction accuracy of the model, but also provided more reliable theoretical support for the application of laser surface melting technology [47].

Chaurasia et al. [7] predicted the temperature distribution within the melt pool and the depth of the melt pool at different laser powers and scanning speeds by means of the finite volume method (FVM) for simulating the LSM process and an FVM model based on the heat conduction equation (HCS). They built a 3D FVM model using ANSYS Fluent, and the numerical domain, associated coordinate system and boundary conditions used in the study are shown in **Fig. 2.11** [48]. The energy equations solved in this study use a moving heat source as a boundary condition to represent the laser

beam, which is modelled as a Gaussian distributed heat source, showing the energy intensity distribution at the different laser powers used in the study.

$$I(x,z) = \frac{2\alpha Q}{\pi r^2} \cdot \exp\left(-2\frac{(x - vt)^2 + Z^2}{r^2}\right) - h(T - T_0) \qquad (2.1)$$
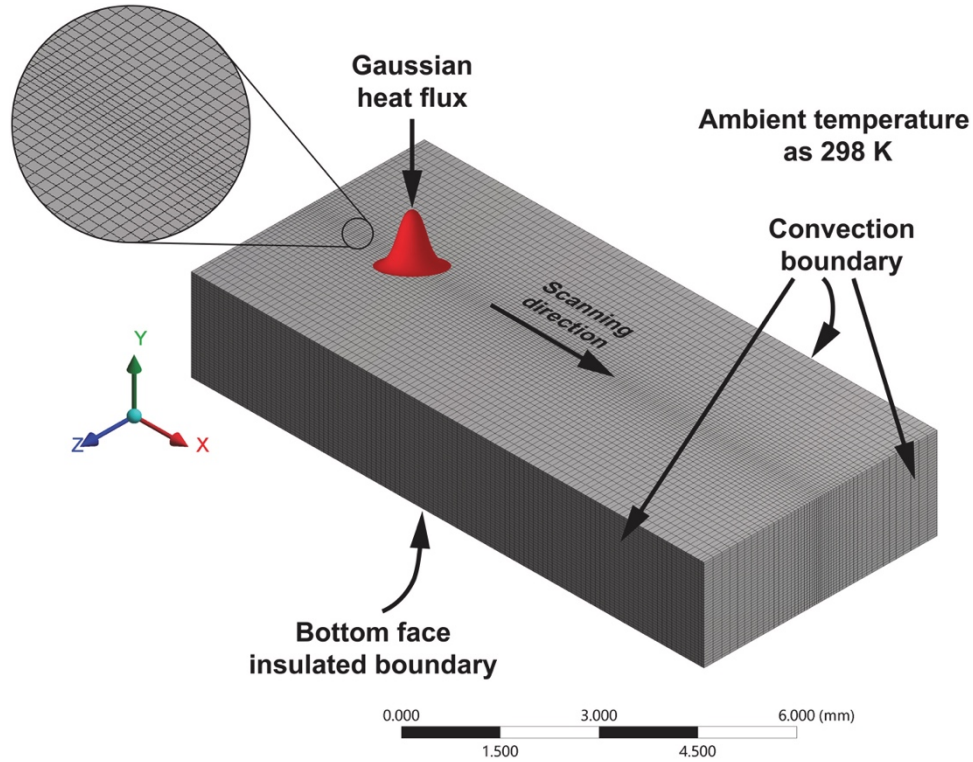
Fig. 2.11 Numerical domain used in the study, related coordinate system and boundary conditions [7].

Fig. 2.11 [7]shows the optical microscopy images of the cross-section of the melted tracks at different combinations of P and v. The melt pool width (MPW) and melt pool depth (MPD) obtained from the heat conduction equation (HCS), fluid dynamics (HCS-FD) models as well as from the experimental measurements are plotted in **Fig. 2.12**a and **Fig. 2.12**b [48] respectively. It can be observed from **Fig. 2.12**a and **Fig. 2.12**b, that both MPW and MPD increase with the increase in P and decrease with the increase in v [48]. As the laser power increases from 300 to 500 W, MPW increases (**Fig. 2.12**a). This increase can be attributed to the melting of more material along the width direction

23

due to the increase in energy density (ED). The trends in MPD results (**Fig. 2.12**b) are

analogous to that of MPW.
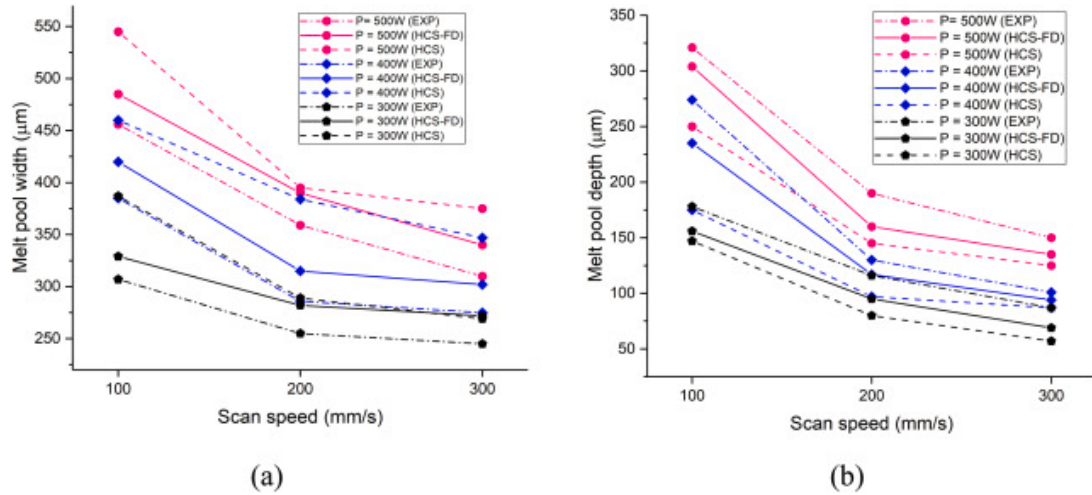
Fig. 2.12 Comparison of experimentally measured (a) melt pool width and (b) melt pool depth with predictions from heat conduction equation (HCS) and fluid dynamics (HCS-FD) models [48].

Results (**Fig. 2.12**a and **Fig. 2.12**b) indicate that both the numerical models used in the

present work are overpredicting the MPW and underpredicting the MPD. The average

error in predictions from the HCS-FD model (9% error in MPW and 12% error in MPD)

was lower when compared to the average error in predictions obtained from the HCS

model (16% error in MPW and 24% error in MPD). The errors in predictions of both

MPW and MPD from the numerical models used herein are comparable to the errors in

predictions from similar numerical models used by other researchers for predicting melt

pool geometry [49, 50]. It can also be seen from **Fig. 2.12**a and **Fig. 2.12**b that the

difference in the magnitude of the predictions made by the two numerical models is

significantly larger at high ED and less at low ED. This can be attributed to the fact that

at high energy density, the temperature gradients are high in the melt pool resulting in

significant change in surface tension from the melt pool to the solidification front leading to strong fluid flow within the melt pool. While for the cases with low ED the temperature gradients are relatively lower and the magnitude of resulting fluid flow is also small. In summary, the predictions of numerical models which consider fluid flow (HCS-FD model) are found to be more accurate than that of HCS model. However, at low energy density, where fluid flow is not significant, the difference in magnitude of the predictions between the two numerical models is also small.

Chaurasia et al. [7] used the finite element method, which does not take into account the liquid and pasty state of the material. taking into account the shape and size of the heat affected zone, the microstructure, and the type of residual stresses, Yeo et al. [51] developed a 3D fully-coupled numerical model reacting to the whole process of laser surface melting. At the top surface, the moving laser heat source and heat loss due to convection and radiation were modeled as follows:

$$k\frac{\partial T}{\partial n} = q_{laser} - h(T - T_0) - \varepsilon\sigma(T^4 - T_0^4) \tag{2.2}$$

where $\partial T/\partial n$, h, ε, σ, and T_0 are the temperature gradient in the surface normal direction, convection heat transfer coefficient, emissivity, Stefan–Boltzmann constant (5.67×10^{-8} W/m^2·K^4), and ambient temperature (20 °C), respectively. For the laser beam, a moving laser heat source with a rectangular top-hat profile, which is the profile used in the experiment, was modeled as

$$q_{laser} = \begin{cases} \frac{\eta P}{L_x L_y}, & for -\frac{L_x}{2} \leq x - U_s t \leq \frac{L_x}{2}, \quad and -\frac{L_y}{2} \leq y \leq \frac{L_y}{2} \\ 0, & for\ others \end{cases} \tag{2.3}$$

Where η is the absorption coefficient, which is a function of the process conditions such as laser power, scanning speed, and shield gas.

Fig. 2.13 shows the simulation results of the experiment, using a larger heat input to examine the effect of melt flow. In **Fig. 2.13** the temperature, normal stress (in the x-direction), and phase distributions are presented at three instances (from top to bottom), and the corresponding velocity fields (top view) are shown at the bottom. In the laser irradiation area, the temperature was above the liquids temperature, and a melt pool was formed. After the laser beam passed, the temperature decreased owing to convective and radiative heat losses and conduction heat transfer.
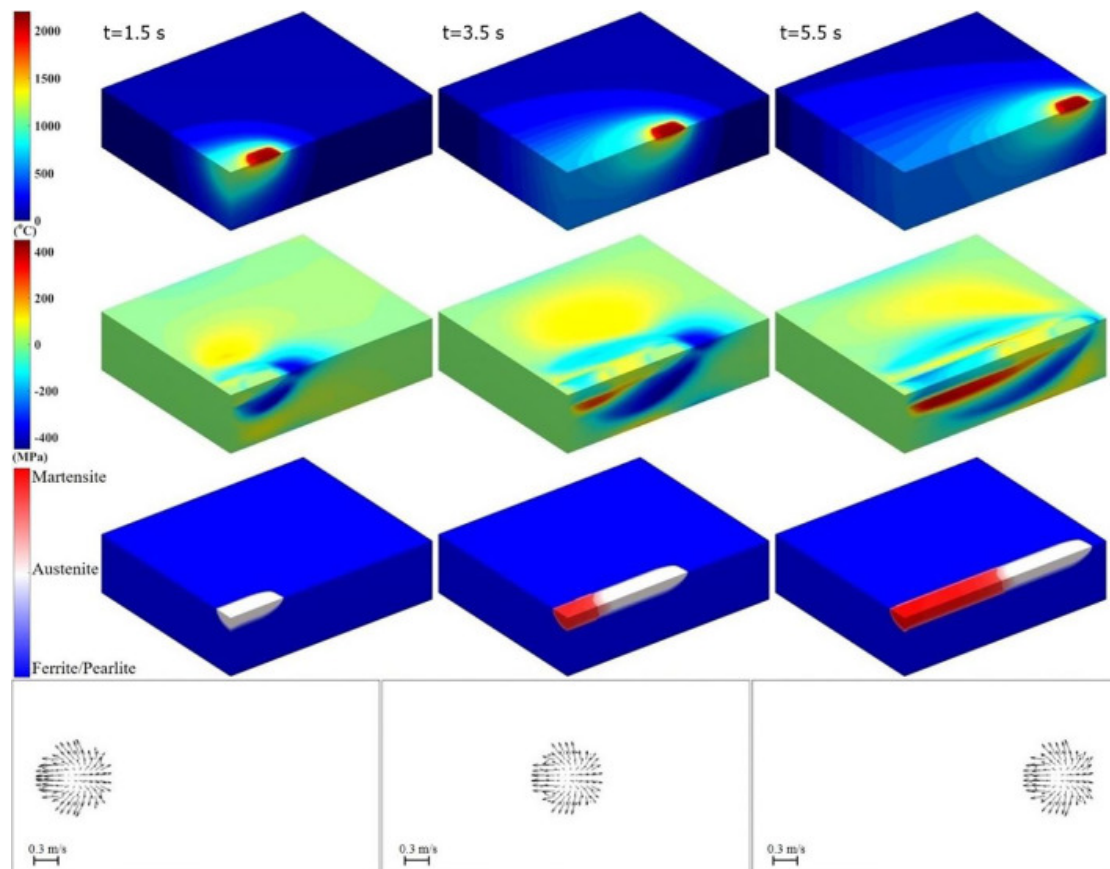
Fig. 2.13 Simulation result for case of maximum heat input. (From top to bottom) Temperature, normal stress in x-direction, solid-state phase, and melt flow at top surface [51].

2.6 Summary

In conclusion, LSM can result in significant changes in microstructure and grain growth behaviour. This advanced technique has proven effective in refining grain sizes, equalizing phase distributions, and triggering beneficial phase transitions. However, research focusing on the evolution of grain boundaries within the melt zone during LSM, particularly the alterations in grain boundary angles, is relatively scarce. This scarcity is attributed to the intricate interplay between laser power and scanning velocity. Unraveling the impact of these parameters on microstructural development and grain growth patterns is essential for attaining refined microstructural control and enhanced process optimization. The objective of this research is to examine the transformations in microstructure and the behavior of grain growth at varying levels of laser power and scanning speeds during the laser surface melting process.

After LSM, the temperature distribution along the laser track axis can predict the melting zone and melt pool depth, and evaluating this temperature distribution is helpful for optimizing laser processing parameters and improving processing quality. While the literature referenced employs software simulations to anticipate the melt pool's thermal profile, these models are quite complicated and require computational software to solve complex equations which is costly and time-consuming. Simplified analytical approach is necessary to predict the melt pool depth more effectively and efficiently.

Chapter 3 Experimental procedure

3.1 Materials

As-cast IN625 rod samples with a 20 mm diameter were cut into button-sized specimens, 10 mm in thickness, by wire electron discharge machining (WEDM, Mitsubishi MV2400). The nominal composition of as-cast IN625 is listed in **Table 3.1**.

Table 3.1 The nominal composition of as-cast IN625.

Element	Ni	Cr	Mo	Nb	Fe	Ti	Al	C
wt%	Bal.	21.5	9.0	3.6	2.5	0.2	0.2	0.2

3.2 Laser surface melting

A schematic diagram of the laser surface melting experimental setup is shown in **Fig. 3.1** (Han's Laser Technology Centre, China). The main components of the system consist of a laser generator, a collimating mirror, a focusing lens, a protective lens and a nozzle. A continuous 2 kW Ytterbium-doped fibre laser (IPG photonics, Germany) operating at 1070 nm wavelength is used as the laser source. The continuous laser beam is generated by the laser generator and reflects off the collimating mirror and towards the focusing lens. The focused laser beam then passes through the protective lens and exits at the nozzle. The sample position was adjusted such that the focal point of the beam was right on the sample upper surface for efficient surface melting. The laser beam diameter (d) is determined by the diameter of fibre (D), focal lengths of collimating mirror (L) and focusing mirror (f), as expressed in Eq. (3.1). D, L, f are found to be 0.1 mm, 100 mm and 500 mm respectively. The laser beam diameter is then calculated to be 500 μm.

$$d = D \times \frac{f}{L} \qquad (3.1)$$
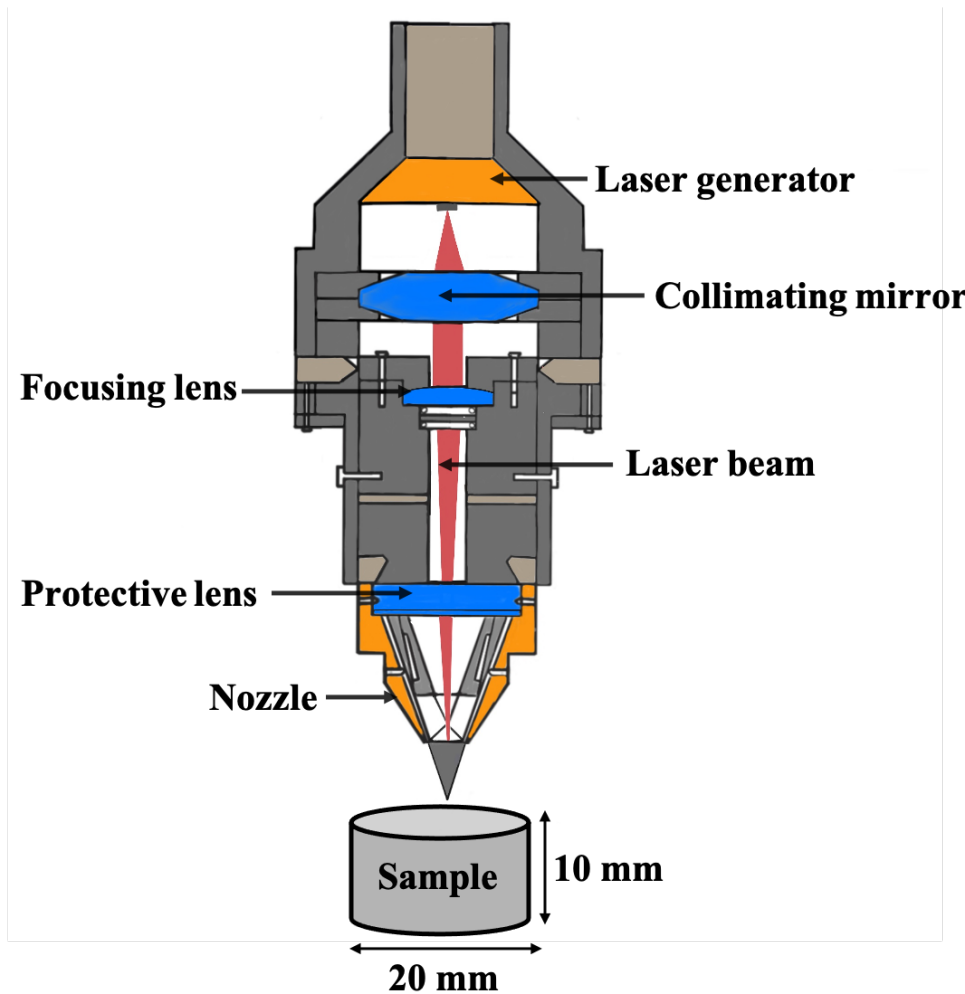
Fig. 3.1 A schematic diagram to show the experimental setup of laser surface melting, consisting of a laser generator, a collimating mirror, a focusing lens, a laser beam, a protective lens and a nozzle.

Prior to laser surface melting, the samples underwent ultrasonic cleaning and degreasing. Then the button-sized IN625 samples were clamped in a self-designed fixture and the laser beam moved linearly across the sample surface in a Zig-Zag trajectory using nitrogen as the shielding gas. A schematic diagram of the laser paths over the surface is depicted in **Fig. 3.2**a. To scan the whole surface, the travel distance of laser track was defined as 25 mm, larger than the sample diameter (20 mm). The hatch spacing between each laser track was 250 μm, which was half of the laser beam

diameter (500 μm) to keep 50 % overlapping ratio between adjacent laser tracks. The processing parameters including laser power and scanning speed are summarised in **Table 3.2**. In preliminary trials, it was found that the melt pool was quite small at a laser power of 200 W and excessive melting occurred at a laser power of 1000 W. To provide sufficient melting and avoid over-melting, the laser power and scanning speed were defined within the range of 400-800 W and 200-800 mm/min respectively. The laser scanning surface was on the XY plane of the sample in **Fig. 3.2**b, where the laser scanned along Y axis at an acceleration and deceleration of 8 m/s^2. The observation surface for microstructure analysis was taken on the XZ plane in the middle of the sample, as highlighted by the red dashed line in **Fig. 3.2**b. The microstructure from the surface to the melt pool boundary was characterised to elucidate the microstructure evolution after laser surface melting, as illustrated in **Fig. 3.2**c.
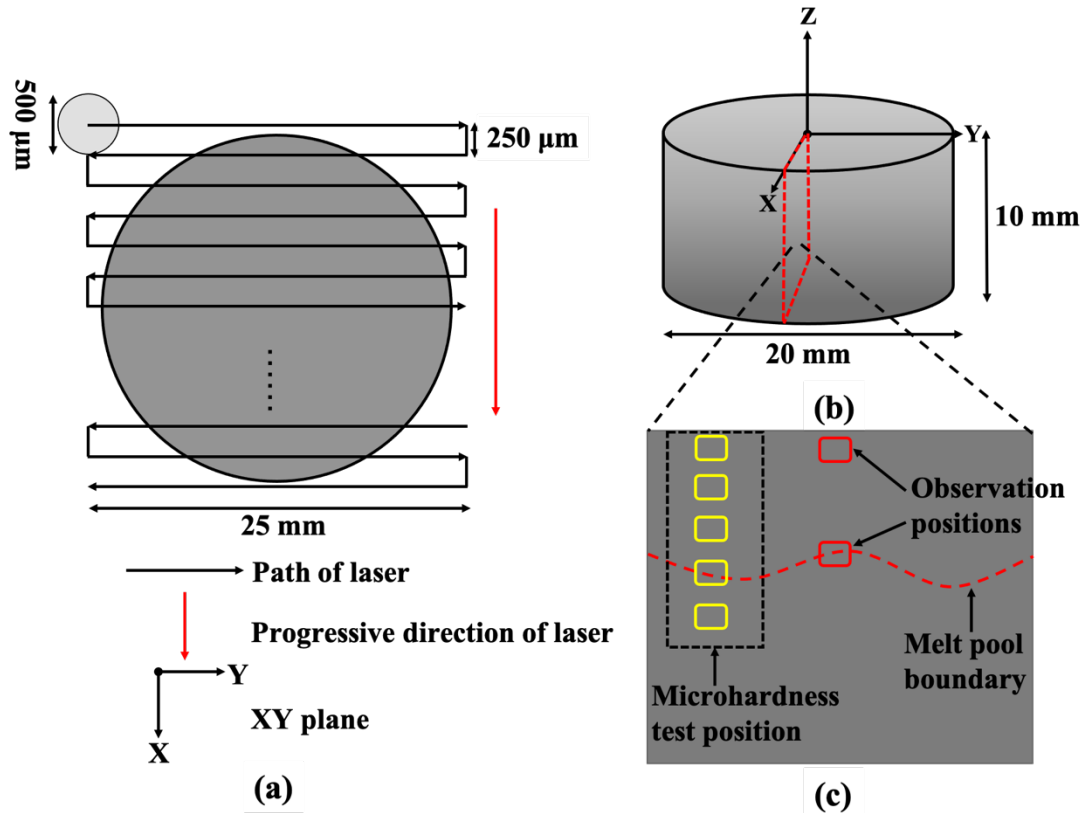
Fig. 3.2 A schematic diagram to show the laser paths over the sample surface with a travel distance of 25 mm for each laser track and a hatch spacing of 250 µm between each track in (a). The XYZ coordinate system of the sample is shown in (b) and the observation positions for cross-sectional microstructures are illustrated in (c) on the XZ plane. The positions for microhardness measurements are also depicted in (c) from the surface towards the base material.

Table 3.2 The processing parameters, including laser power and scanning speed in laser surface melting.

Sample No.	Laser power (W)	Scanning speed (mm/min)	Sample No.	Laser power (W)	Scanning speed (mm/min)	Sample No.	Laser power (W)	Scanning speed (mm/min)
1		200	5		200	9		200
2		400	6		400	10		400
3	400	600	7	600	600	11	800	600
4		800	8		800	12		800

To experimentally verify the target scanning speed can be achieved when the laser scans over the sample surface, a high-speed camera (Phantom VEO 710 L) at a frame rate of 400 frames per second and a resolution of 1280×800 was employed to capture the laser motion at speeds of 200-800 mm/min for a travel distance of 25 mm. It is found that the actual scanning speed reaches the target speed in a very short period (less than one frame interval) and remains identical to the target speed from 0 to 25 mm, meaning that the acceleration and deceleration is very high in the laser scanning process. Since the travel distance of laser track is 25 mm and the sample diameter is 20 mm, the target speed has long been achieved when the laser beam starts to contact the sample.

To represent the combination effect of laser power and scanning speed on the laser treated sample, the area energy density (AED) was calculated since only surface melting occurred during this process, which is expressed in Eq. (3.2) [52],

$$AED = \frac{P}{vH} \tag{3.2}$$

Where P is the laser power in W, v is the scanning speed in mm/s and H is the hatch spacing between each laser track in mm, and the AED is given in J/mm^2. **Fig. 3.3** summarizes the AED using the laser power and scanning speeds in **Table 3.2**. It can be clearly seen that the AED increases with laser power and decreases with scanning speed (The region for the cellular structure formation in **Fig. 3.3** will be detailed in Section 3.4).
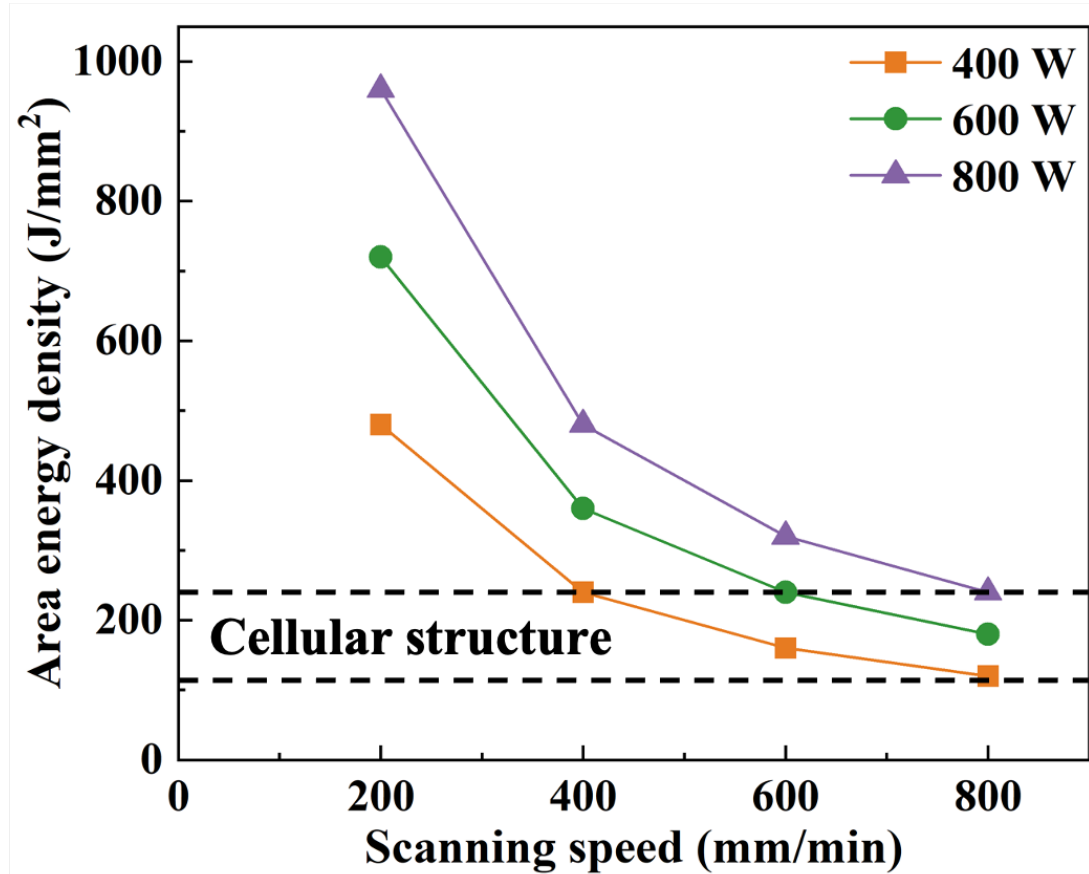
Fig. 3.3 The plot of area energy density against scanning speed at laser power of 400 W, 600 W and 800 W. The range of energy density to produce the cellular structure after laser surface melting in highlighted.

3.3 Microstructure characterisation

After laser surface melting, samples were cut by EDM and XZ cross-sections (according to **Fig. 3.2**b) were mounted in a conductive resin and successively ground and polished to 5 μm and 1 μm surface finish using diamond suspensions and eventually to 0.04 μm surface finish using colloidal silica suspension. The microstructure of the cross-sections after laser surface melting was characterized by a field emission scanning electron microscope (FEG-SEM, ZEISS Sigma VP) using backscattered electron (BSE) imaging at an accelerating voltage of 15 kV and a working distance of 8 mm. The phase composition was semi-quantitatively analyzed by energy dispersive X-ray spectroscopy

(EDS). The grain structure of as-cast and laser surface melted IN625 alloys were characterized by electron backscattered diffraction (EBSD) at an accelerating voltage of 15 kV and a beam current of 3.57 nA with a specimen tilt angle of 70° (JEOL 7100 F FEG-SEM with an EBSD detector, Oxford Instruments). Areas of around 800×600 μm^2 from the melted region to the bulk material were selected for EBSD mapping at a step size of 0.5 μm to show the transition of grain structure after laser surface melting. X-ray diffraction (XRD, Bruker D8 Advance) was performed in a 2θ range from 20°-120° at 5°/min for phase identifications. Vickers microhardness measurements (Buehler VH3300) were performed from the top of the melt zone towards the base material (**Fig. 3.2**c) using a Vickers indenter at 300 gf and a dwell time of 20 s. The spacing between each indent was 50 100 μm to avoid work hardening effect from adjacent indents. The surface roughness, Ra, after laser surface melting is measured by a 2D profilometer (MarSurf GD 120).

Chapter 4 Results and discussion

4.1   As-cast microstructures

Fig. 4.1 shows the BSE-SEM micrographs of as-cast IN625 prior to laser surface melting, where **Fig. 4.1**a was taken at a low magnification to show the overall structure and **Fig. 4.1**b was an enlarged view of the highlighted area in **Fig. 4.1**a. It can be seen from **Fig. 4.1**a that the as-cast IN625 exhibits a single γ-Ni phase structure with some bright-contrast precipitates and dark-contrast impurities embedded in the γ matrix. These bright-contrast precipitates are the niobium carbides (NbC) and the dark-contrast impurities are the Ti/Nb-rich nitrides, as confirmed by the EDS results in **Table 4.1**. The micron-sized niobium carbides exhibit a rod-shaped morphology and are distributed evenly in the γ matrix, of which the area fraction is around 1%. The discrete (Ti, Nb)N nitrides are likely resulted from the casting process with an area fraction less than 1%. The presence of the NbC and (Ti, Nb)N in the as-cast IN625 has also been reported in the literature, which shows a good agreement with the phase structure observed in **Fig. 4.1** [53].
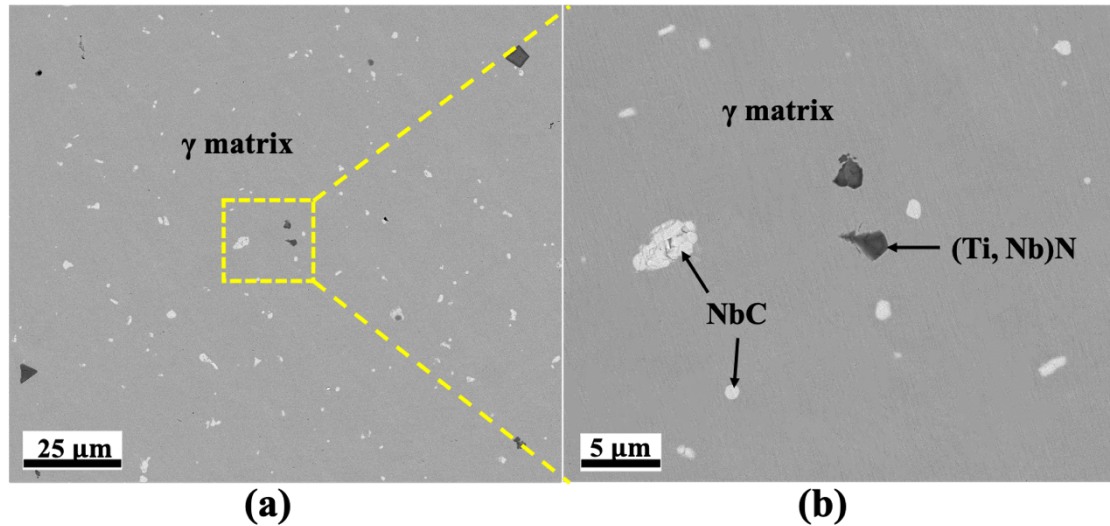
Fig. 4.1 A low magnification BSE-SEM micrograph to show the single γ-phase structure (a) and a high magnification BSE-SEM micrograph to depict the Nb-rich carbides and Ti/Nb-rich nitrides (b) in the as-cast IN625.

Table 4.1 The composition of γ phase, Nb-rich carbides and Ti/Nb-rich nitrides in as-cast IN625.

Element (wt%)	C	Ti	Cr	Ni	Nb	Mo	N	Fe
γ phase	5.1	---	21.1	60.5	1.6	7.2	---	4.5
Nb-rich carbides	17.2	1.6	1.3	1.7	75.2	3.0	---	---
Ti/Nb-rich nitrides	3.6	50.1	5.2	---	24.8	---	16.3	---

The grain structure of as-cast IN625 is shown in **Fig. 4.2**, where **Fig. 4.2**a is the band contrast image to show the grain morphology, **Fig. 4.2**b is the inversed pole figure (IPF) mapping to show the grain orientations and **Fig. 4.2**c is the phase mapping. It can be seen that the as-cast IN625 exhibits a polycrystalline structure with equiaxed grains in **Fig. 4.2**a. The grain size is measured to be around 4.5 μm by image analysis. No preferred grain orientation can be found in **Fig. 4.2**b, showing the homogenous grain

structure of IN625 in the as-cast condition. Twinned grains with clear twin boundaries are also observed in **Fig. 4.2**b representing the typical grain structure of as-cast IN625. It is confirmed by **Fig. 4.2**c that the as-cast IN625 exhibits a predominantly single γ-fcc structure. The corresponding grain boundary mappings at misorientations below 15°, 15-49° and above 49° are shown in **Fig. 4.2**d, **Fig. 4.2**e and **Fig. 4.2**f respectively. It is seen that the small angle grain boundaries are quite limited in **Fig. 4.2**d. The fraction of medium and large angle grain boundaries is almost the same, 50%. It is also seen clearly that the large angle grain boundaries are mainly the twin boundaries in **Fig. 4.2**f.
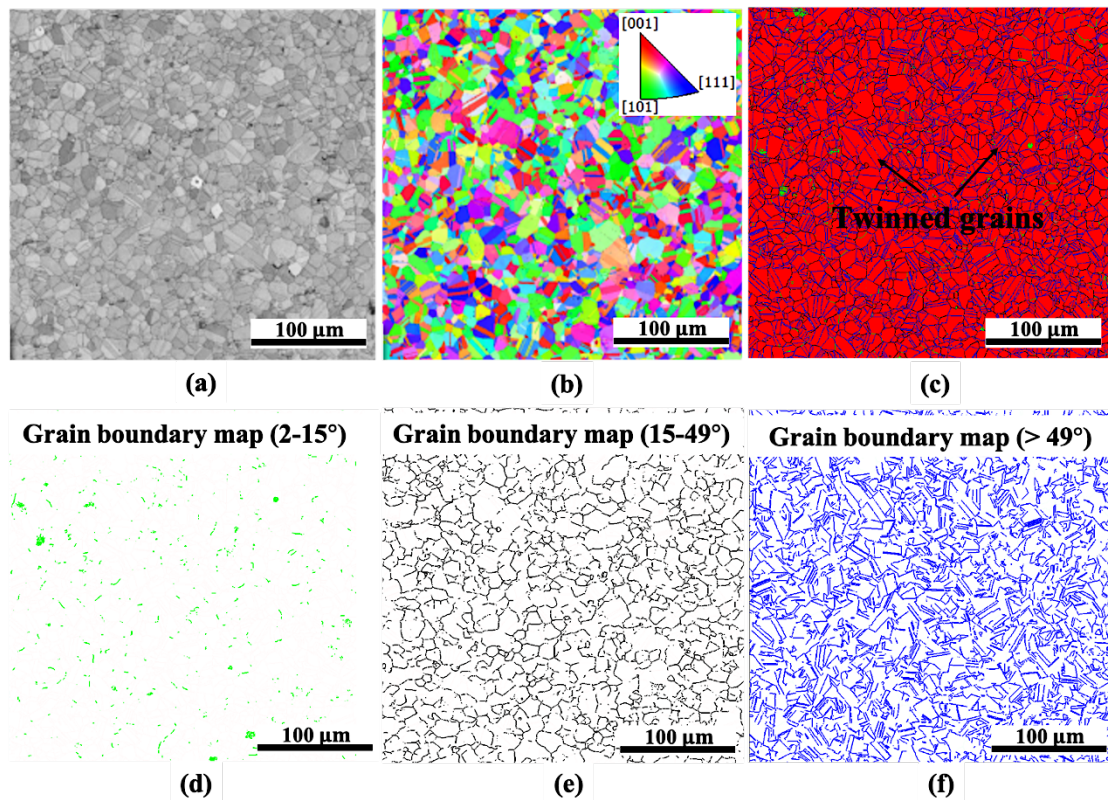
Fig. 4.2 The EBSD mapping of as-cast IN625: band contrast image (a), inversed pole figure (IPF) mapping (b), phase mapping (c), grain boundary mapping for misorientations <15° (d), grain boundary mapping for misorientations 15°-49° (e) and grain boundary mapping for misorientations >49° (f).

4.2   Laser surface melting at 400 W

Fig. 4.3 presents the microstructure evolution of IN625 after laser surface melting at a laser power of 400 W and scanning speeds from 200 mm/min to 800 mm/min. At low scanning speed of 200 mm/min, it can be seen that some dark-contrast and micron-sized oxides are formed within the melt pool in **Fig. 4.3**a. These oxides are randomly distributed in the melt pool with a spherical morphology and are identified as aluminium oxides by EDS analysis in **Table 4.2**. It is likely due to the fact that the low scanning speed allows sufficient time for the oxidation reaction to occur, forming stable aluminium oxides in the melt pool during the melting-solidification process. The area fraction of these oxides is measured to be around 1% and they are distributed throughout the melted region towards the melt pool boundary in **Fig. 4.3**b. Some light-contrast secondary phases start to precipitate from the γ matrix, as seen from **Fig. 4.3**b. These secondary phases, which exhibit a slightly lighter contrast compared to the γ matrix, are due to the segregation of heavy elements during solidification. Similar phenomena have been reported in the literature [54], consistent with **Fig. 4.3**b. When the scanning speed is 400 mm/min, the secondary phases become more visible and exhibit a cellular structure, as in **Fig. 4.3**c, during the rapid laser surface melting and solidification of the alloy, microstructures with cellular features are formed due to the segregation of heavier elements such as Nb. Within the secondary phases, some bright precipitates are found in **Fig. 4.3**. These precipitates are believed to be the Laves phase that is rich in Ni and Nb, of which the EDS composition is shown in **Table 4.3**. The Laves phases are mainly distributed within the secondary phase due to sufficient

segregation of heavier elements such as Nb, Mo. Less Laves phase can be found near the melt pool boundary, as seen from **Fig. 4.3**d. This is due to that the melted region near the bulk material experiences more rapid solidification compared to that near the surface of the melt pool. The segregation of heavy elements is thus not very significant in **Fig. 4.3**d and the Laves phase can hardly form. But solidification near the surface is relatively slower compared to the region near the melt pool boundary, this gives enough time for the element segregation, resulting in the formation of Laves phase in **Fig. 4.3**c.
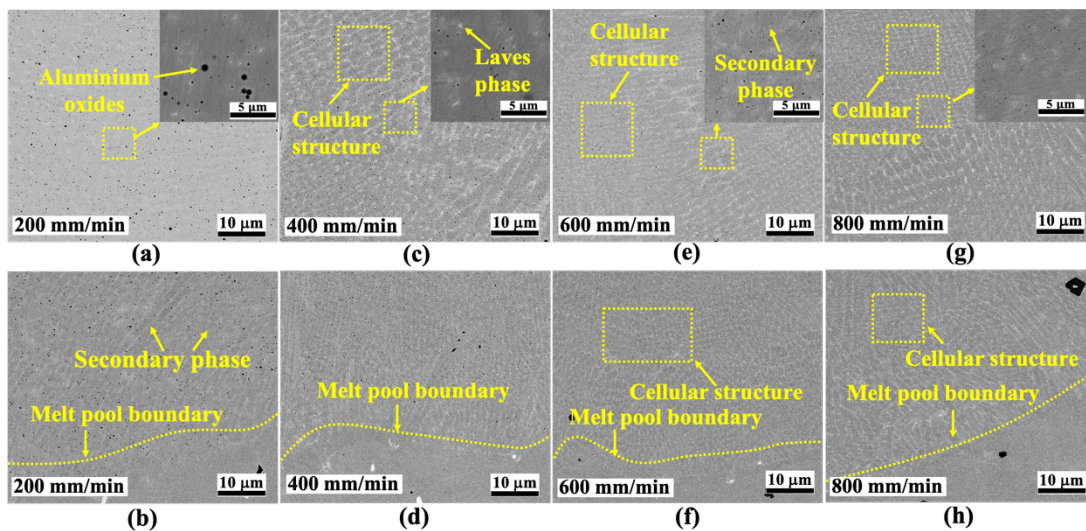
Fig. 4.3 BSE-SEM micrographs of IN625 after laser surface melting at a laser power of 400 W to show the microstructure near the surface and near the melt pool boundary at scanning speed of 200 mm/min (a and b), 400 mm/min (c and d), 600 mm/min (e and f) and 800 mm/min (g and h).

Table 4.2 Elemental composition of the oxides.

Element (wt%)	C	O	Al	Ti	Cr	Fe	Ni	Mo
Oxides	7.0	26.5	23.3	8.2	12.4	1.7	17.4	3.5

Table 4.3 Elemental composition of the Laves phase.

Element (wt%)	C	Ti	Cr	Ni	Nb	Mo
Laves phase	5.5	1.8	15.3	43.4	14.8	19.2

When the scanning speeds increase to 600 mm/min and 800 mm/min, a refined cellular structure is seen in **Fig. 4.3**e and **Fig. 4.3**g, in which the size of the cells decreases as compared to that in **Fig. 4.3**c. It is reported that the formation of cellular structure is governed by the thermal gradient in the melt pool [55]. At the laser power of 400 W, the energy density decreases with scanning speed, leading to less heat input and more rapid solidification at higher scanning speeds. This restricts growth of cellular structure and a refined cellular structure is thus formed in **Fig. 4.3**e and **Fig. 4.3**g. The bulk material still exhibits a single γ phase structure. This refined cellular structure is also similar to those reported in selective laser melting (SLM) of Ni-based alloys [56]. In SLM, the growth of cellular grain can be in different directions since rotational scanning strategies are often used. Laser surface melting is similar to SLM, but instead of melting powders, bulk material is melted without rotation of the laser scanning directions. As a result, the cellular grains tend to grow in the same direction. This is indeed evidenced from **Fig. 4.3**, where the cross sections of the cells can be seen. It is also noted that the amount of oxide inclusions in **Fig. 4.3**c to **Fig. 4.3**g is much less compared to that in **Fig. 4.3**a when the scanning speed increases. At low scanning speed (200 mm/min) with high energy density, the melted region needs more time to solidify. This gives further exposure of the molten material to oxygen at high temperatures, even

though nitrogen shielding gas is provided. Consequently, more oxide inclusions are formed in **Fig. 4.3**a, whilst rapid solidification at higher scanning speeds limits the oxidation of the melt pool. This is evidenced from **Fig. 4.3**c and **Fig. 4.3**e, where the oxide inclusions gradually decrease, and a dense structure free of oxide inclusions is seen in **Fig. 4.3**g.

4.3   Laser surface melting at 600 W

Fig. 4.4 depicts the microstructure evolution of IN625 after laser surface melting at a laser power of 600 W and scanning speeds from 200 mm/min to 800 mm/min. Similar to **Fig. 4.3**a, oxide inclusions are also seen in **Fig. 4.3**a at the scanning speed of 200 mm/min. The secondary phase due to heavy element segregation starts to form in **Fig. 4.4**a. The microstructure of the bulk material below the melt pool boundary remains almost unchanged, with discrete Nb-carbides and Ti/Nb-nitrides as shown in **Fig. 4.4**b. When the scanning speed increases to 400 mm/min, the secondary phase becomes more visible (**Fig. 4.4**c). Some discrete Laves phases are also found due to the segregation of Nb. It is noticed that the bulky NbC particles near the melt pool boundary have been refined into small ones in **Fig. 4.4**d. This is because the bulky NbC particles undergo an incomplete dissolution into small particles when the laser power increases.
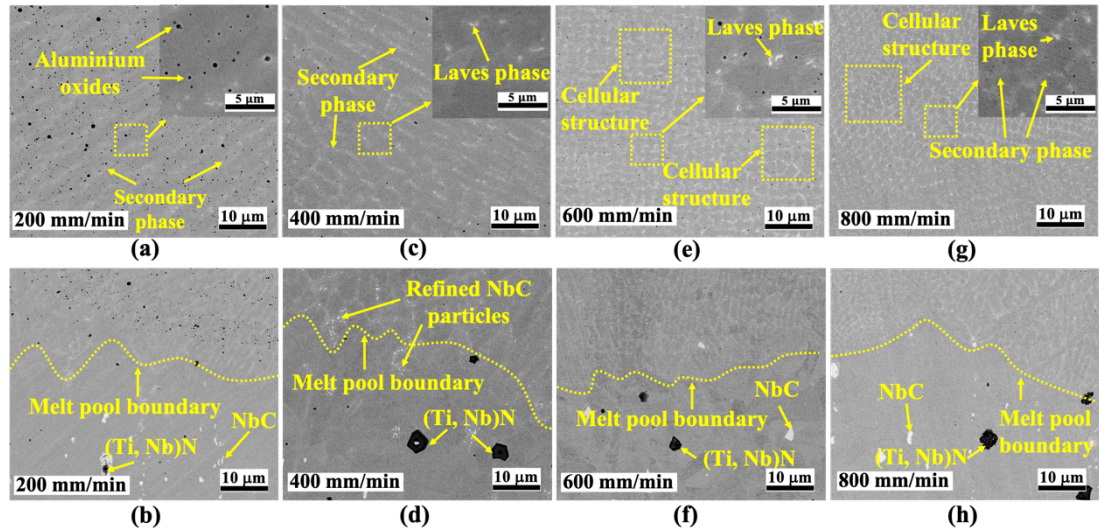
Fig. 4.4 BSE-SEM micrographs of IN625 after laser surface melting at a laser power of 600 W to show the microstructure near the surface and near the melt pool boundary at scanning speed of 200 mm/min (a and b), 400 mm/min (c and d), 600 mm/min (e and f) and 800 mm/min (g and h).

The typical cellular structure with a more homogenous distribution of the secondary phase and Laves phase can be seen in the **Fig. 4.4**e and **Fig. 4.4**g. Since the energy density decreases with the scanning speed, more rapid solidification is thus expected in **Fig. 4.4**e and **Fig. 4.4**g. This means the nucleation and growth of dendrites are more significant at high scanning speeds [57], and subsequently, a cellular structure is obtained. Similar findings have also been reported in previous work [58], which shows a good consistency with this work. In the bulk material, the single γ phase structure with discrete Nb-carbides and Ti/Nb-nitrides is retained below the melt pool boundary in **Fig. 4.4**f and **Fig. 4.4**h. The partial dissolution of Nb-carbides is not found, which is because the reduced energy density at 600 mm/min and 800 mm/min provides insufficient heat input for the dissolution of Nb-carbides.

4.4   Laser surface melting at 800 W

Fig. 4.5 shows the microstructure evolution of IN625 after laser surface melting at a laser power of 800 W and scanning speeds from 200 mm/min to 800 mm/min. Oxide inclusions are found in **Fig. 4.5**a, which is similar to **Fig. 4.3**a and **Fig. 4.4**a. It further indicates that the slow scanning speed of 200 mm/min gives sufficient time for the molten metal to contact with oxygen and allows the oxide inclusions to form within the melt pool. The formation of the secondary phase and Laves phase can be seen in **Fig. 4.5**c and **Fig. 4.5**e. A very high energy density is resulted from the increased laser power at 800 W (see **Fig. 3.3**). The increased energy density in **Fig. 4.5**a-**Fig. 4.5**e provides more heat input and allows the precipitation of secondary phase and Laves phase in the γ matrix. Increased laser power input results in higher peak temperatures within the molten pool, and the enhanced dissolution of Nb at elevated temperatures facilitates the development of laves phases, leading to a greater quantity of laves phases being produced at 800W.Partial melting of the Nb-rich carbides is also noticed near the melt pool boundary from **Fig. 4.5**b-**Fig. 4.5**f, and some Ti/Nb-rich nitrides are noted in the bulk material in **Fig. 4.5**b and **Fig. 4.5**d.
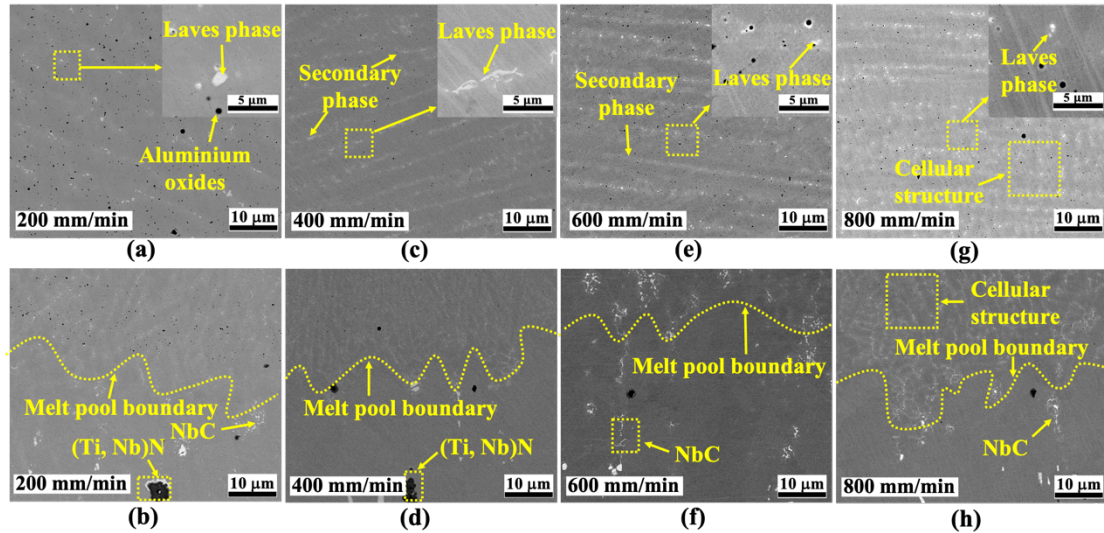
Fig. 4.5 BSE-SEM micrographs of IN625 after laser surface melting at a laser power of 800 W to show the microstructure near the surface and near the melt pool boundary at scanning speed of 200 mm/min (a and b), 400 mm/min (c and d), 600 mm/min (e and f) and 800 mm/min (g and h).

When the scanning speed increases to 800 mm/min, the area fraction of the light-contrast secondary phase increases, indicating more segregation of heavy elements and precipitation of Laves phase. A cellular structure is obtained in **Fig. 4.5**g, which is similar to the structure in **Fig. 4.4**e. It should be noted that the energy density of **Fig. 4.5**g is almost identical to that in **Fig. 4.4**e. Given that the cooling conditions are almost the same in all the laser treatments, the higher energy densities will produce a larger melt pool, followed by longer solidification time, which allows further growth of the secondary phase with a wide distribution. But at a low energy density (i.e. scanning speed at 800 mm/min), the solidification time reduces, and segregation of heavy elements is restricted, forming the cellular structure as shown in **Fig. 4.5**g. It is also seen from the bulk material in **Fig. 4.5**f that more dissolution of the Nb-carbides occurs due to the large laser power (800 W) used in this case. It is reported by Antonsson et al. [58] that the solubility of Nb in the primary γ phase increases with temperature. At the

laser power of 800 W, the temperature in the melt pool in much higher than that at 400 W and 600 W, resulting in more dissolution of NbC, as indeed seen in **Fig. 4.5**f and **Fig. 4.5**h in the bulk material. The cellular structure formation can be summarised from **Fig. 4.3**, **Fig. 4.4** and **Fig. 4.5**: cellular structures are formed when the area energy density is ≤ 240 J/mm^2 as indicated in **Fig. 3.2**. It is further evidenced by **Fig. 4.3**c, **Fig. 4.4**e and **Fig. 4.5**g that the cellular structure is firstly observed in these conditions where the energy density is 240 J/mm^2. And when the energy density decreases, refined cellular structures are obtained, as supported by **Fig. 4.3**e, **Fig. 4.3**g and **Fig. 4.4**g XRD results of the all the laser surface melted samples are shown in **Fig. 4.6**. It can be seen that the laser treated samples still exhibit a primary γ phase structure, without significant phase changes. The Laves phase and carbides can hardly be detected due to their small amounts. Some oxides are found to exist when the laser power increases, which agrees well the oxide inclusions seen in **Fig. 4.3**, **Fig. 4.4** and **Fig. 4.5**.

The XRD peaks for the 400 W, 600 W and 800 W samples are plotted in **Fig. 4.6** to compare the phase formation after laser surface melting. It can be seen that the laser treated samples still exhibit a primary γ phase structure, without significant phase changes. The different peaks obtained in the XRD analysis indicate the presence of metal carbides (MC), along with the γ-Ni matrix. Apart from this, the intermetallic phases such as Laves phase, which were generally obtained for the conventionally processed IN625 sample, were not detected by the XRD. The microstructures are the same as the SLM state and all of them are the solution of Cr in Ni matrix. The intermetallic phases such as γ'' (Ni$_3$Nb), δ (Ni$_3$Nb), which can usually be found in

casting and forging but are not detected in the XRD results because the sizes of these

particles are small [59]. This can be attributed to their small size and volume fraction.
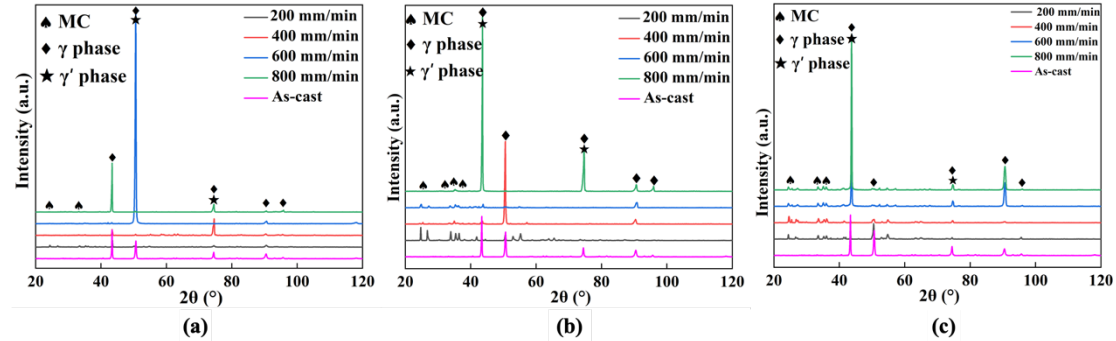
Fig. 4.6 XRD results of as-cast and laser surface melting IN625 at 400 W (a), 600 W (b) and 800 W (c).

It has to be mentioned that power density instead of energy density was also used in

previous studies to represent power input in laser surface melting [60]. High power

density within a short interaction/pulse time or low power density within a long

interaction/pulse time can both produce the same energy density but induce either

surface hardening or surface melting [61]. Considering that the laser beam diameter is

a constant (500 μm) and only surface melting occurs for all the alloy samples, as seen

from **Fig. 4.3**, **Fig. 4.4** and **Fig. 4.5**, the energy density thus is used as a reasonable

indicator to represent the combination effects of laser power and scanning speed.

4.5   Grain growth characteristics

To investigate the grain growth behaviour in laser surface melting, EBSD analysis is

performed on selected samples to elucidate the effects of laser power and scanning

speed on the grain structure characteristics. It is seen previously from **Fig. 4.3**, **Fig. 4.4**

and **Fig. 4.5**, that oxide inclusions are found to exist at low scanning speeds and typical

cellular structures are formed at relatively high scanning speeds of 600 mm/min and

800 mm/min. Since the laser power has a dominant effect on the melt pool depth and grain growth behaviour, grain structure characteristics at different laser powers are thus compared at 600 mm/min and 800 mm/min. The EBSD clearly shows the texture of the samples. **Fig. 4.7- Fig. 4.9** and **Fig. 4.13 - Fig. 4.15** are the inverse pole figure (IPF) of the X-Z section, in which a region with a single color represents the presence of one grain only. Hence, some larger elongation grains of several hundred micrometers in length grow cross a few layers. A very strong texture can be identified for the LSM sample. The long axes of most of the grains are aligned in the <001> direction and a cube texture is observed in the X-Z section. This phenomenon was also observed by other researchers [62]. Inconel 625 has a face-centered cubic crystal structure. The preferred orientation is <001> [63]. During the LSM process, the laser melts the powder on the top of the sample but the substrate or the layer that has solidified still remains cold. So, the temperature gradient forms from the top to the bottom. The dendrites get the priority to grow; as a result, the angle between <001> and the direction of heat flux is minimum. Meanwhile, the maximum temperature in the molten pool can reach 4500 K [64], leading to superheat. These further result in the difficulty to form homogeneous nucleation in the molten pool, which can enhance the growth of columnar crystal in the molten pool. Under this condition, the columnar grain will grow from the bottom of the molten pool towards the top. However, the interaction of the laser and powder, liquid metal, surrounding atmosphere, solidified base metal and un-melted metal powders can collaboratively form a large temperature gradient, which may result in surface tension gradient and Marangoni convection [65]. The velocity of convection flow in the melt

pool can reach tens of meter per second according to the simulation result [66]. The convection in the molten pool can break the original growth law of columnar crystal. Parts of dendrites change growth directions, causing the formation of steering dendrite. Thus, some grains change the grow directions rather than always being towards <001>. **Fig. 4.7**, **Fig. 4.8** and **Fig. 4.9** shows the grain structure evolution of IN625 after laser surface melting at laser power from 400 W to 800 W under a constant scanning speed of 600 mm/min. The grain size is measured to around 11 μm, 14 μm and 16 μm at 400 W, 600 W and 800 W respectively in the melted region, showing an obvious grain growth behaviour in comparison to the initial grain size of 4.5 μm in the as-received IN625. It can be seen from **Fig. 4.7**a and **Fig. 4.7**b that some coarse grains are formed at the surface of the melted region. In the middle of the melted region, the grains exhibit a tendency to grow towards the surface, which indicates that the solidification direction is from the substrate to the melt pool surface. Most grains are randomly oriented and no preferred grain orientations can be found in **Fig. 4.7**b. The twinned grains which are a typical feature in the bulk material can be seen in **Fig. 4.7**b, but no twinned grains can be found in the melted region. This is likely due to that the rapid heating and cooling during laser surface melting restricts the formation of twinned grains and allows some columnar grains to grow towards the surface [62]. The phase mapping in **Fig. 4.7**c indicates that the alloy still exhibits a primary γ-fcc phase structure after laser surface melting. Similarly, coarse grains are also found in **Fig. 4.8**a and **Fig. 4.8**b near the surface of the melt pool. The columnar grains are seen more obviously in **Fig. 4.9**a and **Fig. 4.9**b when the laser power increases to 800 W. It is understood that the energy

density increases with laser power at a constant speed, as shown previously in **Fig. 3.3**. Thus, the solidification time becomes longer when the laser power increases, allowing the columnar grains to grow from the melt pool boundary towards the surface, as supported by **Fig. 4.9**a and **Fig. 4.9**b. The overall phase structure remains a single γ phase structure, as shown in **Fig. 4.8**c and **Fig. 4.9**c. In addition to this, we also observed and analysed the pole figures of IN625 after laser surface melting, and the grain orientation did not change significantly, which indicates that the grain orientation remains relatively consistent before and after laser surface melting. The corresponding grain boundary mappings at misorientations below 15°, 15-49° and above 49° are depicted in **Fig. 4.10**, **Fig. 4.11** and **Fig. 4.12**. The melted region mainly consists of medium angle grain boundaries with an area fraction around 90%. The large angle grain boundaries can hardly be found in the melted region. Since twin boundaries usually have a grain boundary misorientation of 60°, large angle grain boundaries were seen previously in the as-cast IN625 (**Fig. 4.2**). But after laser surface melting, the twinned grains are not able to form in the melted region and large angle grain boundaries are thus not found.
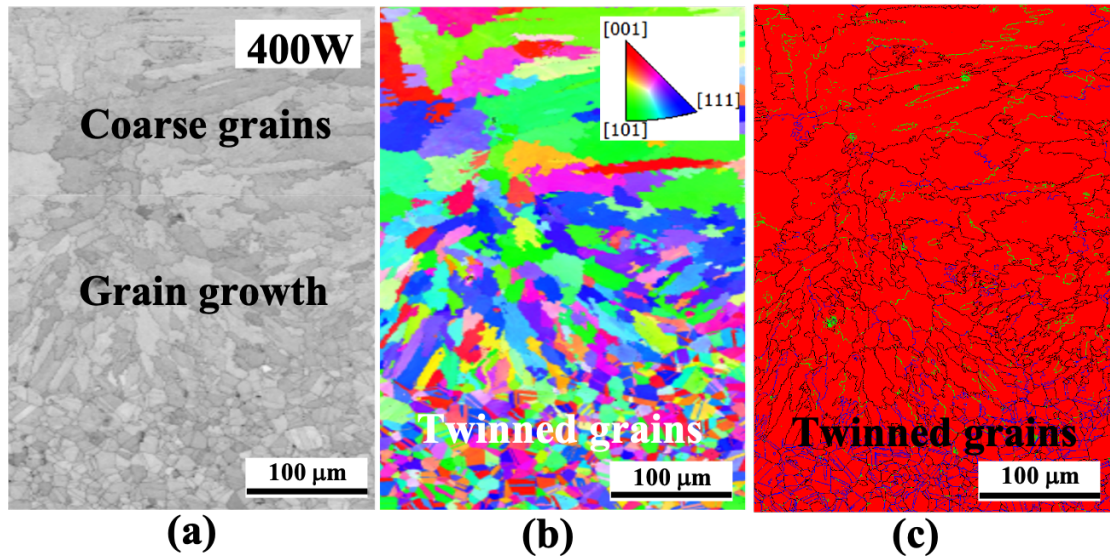
Fig. 4.7 EBSD mappings of the IN625 after laser surface melting at a scanning speed of 600 mm/min with laser power of 400 W. Figures from left to right are band contrast image (a), inversed pole figure (IPF) (b) and phase mapping (c).

Fig. 4.8 EBSD mappings of the IN625 after laser surface melting at a scanning speed of 600 mm/min with laser power of 600 W. Figures from left to right are band contrast image (a), inversed pole figure (IPF) (b) and phase mapping (c).

Fig. 4.9 EBSD mappings of the IN625 after laser surface melting at a scanning speed of 600 mm/min with laser power of 800 W. Figures from left to right are band contrast image (a), inversed pole figure (IPF) (b) and phase mapping (c).
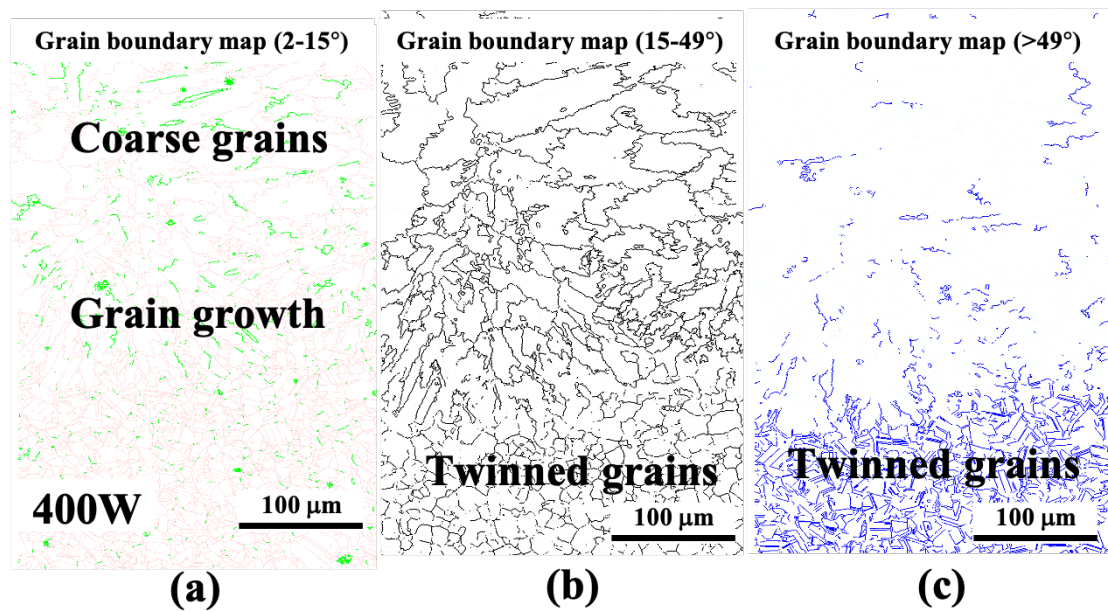
Fig. 4.10 Grain boundary mapping a scanning speed of 600 mm/min with laser power of 400 W. Figures from left to right are grain boundary maps at misorientations <15° (a), 15-49° (b) and >49° (c).

Fig. 4.11 Grain boundary mapping a scanning speed of 600 mm/min with laser power of 600 W. Figures from left to right are grain boundary maps at misorientations <15° (a), 15-49° (b) and >49° (c).

Fig. 4.12 Grain boundary mapping a scanning speed of 600 mm/min with laser power of 800 W. Figures from left to right are grain boundary maps at misorientations <15° (a), 15-49° (b) and >49° (c).

Fig. 4.13, **Fig. 4.14** and **Fig. 4.15** depicts the grain growth behaviour of IN625 after laser surface melting at a constant scanning speed of 800 mm/min and a laser power from 400 W to 800 W. A similar grain size of about 14 μm is found in all the samples

in **Fig. 4.13**, **Fig. 4.14** and **Fig. 4.15** Together with **Fig. 4.7**, **Fig. 4.8** and **Fig. 4.9** it can be seen that the impact on grain size is dominated by the laser power at low scanning speeds. But when the scanning speed is sufficiently high (**Fig. 4.13**, **Fig. 4.14** and **Fig. 4.15**), the effects of laser power on the grain size are quite limited since the high scanning speeds give a more rapid solidification, restricting the further grain growth. This is also consistent with the findings in the previously reported work [38]. At low laser power (400 W), coarse grains are found near the surface in **Fig. 4.14**a and **Fig. 4.14**b, which is similar to that in **Fig. 4.7**a and **Fig. 4.7**b. Below the coarse grain region, some elongated grains are also seen. The equiaxed grains with twins are observed in the base material at the bottom of **Fig. 4.13**b and a single γ phase structure is maintained in **Fig. 4.13**c. When the laser power increases from 400 W to 600 and 800 W, the columnar grains can be seen clearly between the coarse grain region and the base material. This columnar grain region, of approximately 200 μm in depth, demonstrates that the grains tend grow from the base material towards to surface of the melt pool. Similar to **Fig. 4.7** - **Fig. 4.9**, no twinned grains can be found in the melted region. It is noted that the columnar grains are not yet formed in **Fig. 4.13**a and **Fig. 4.13**b. This is likely because the laser power is relatively low at 400 W and the depth of the melt pool is quite limited at high scanning speeds (i.e. 800 mm/min). The shallow melt pool depth limits the growth of columnar grains. When the power increases to 600 W and 800 W, the melt pool size and depth increase with the laser power, allowing sufficient time for columnar grains to grow from the melt pool boundary towards the surface, like **Fig. 4.14** and **Fig. 4.15**. The corresponding grain boundary mappings at misorientations

below 15°, 15-49° and above 49° are presented in **Fig. 4.16** -**Fig. 4.18**. Like **Fig. 4.10** to **Fig. 4.12**, it can be seen that the melted region mainly consists of medium angle grain boundaries with an area fraction above 90 %. It is seen from **Fig. 4.10** - **Fig. 4.12**, that no twinned grains can be found in the melted region and thus large angle grain boundaries can hardly be found in the melted region. In the grain boundary mappings of **Fig. 4.10** - **Fig. 4.12** and **Fig. 4.16** - **Fig. 4.18**, a large area fraction (over 90 %) of medium angle grain boundaries is seen in the melted region. It is understood that the fraction of medium angle grain boundaries is related to the grain size. Since no significant difference in grain size can be found from **Fig. 4.7** - **Fig. 4.9**, **Fig. 4.13** - **Fig. 4.15**, similar fractions of medium angle grain boundaries are thus obtained.
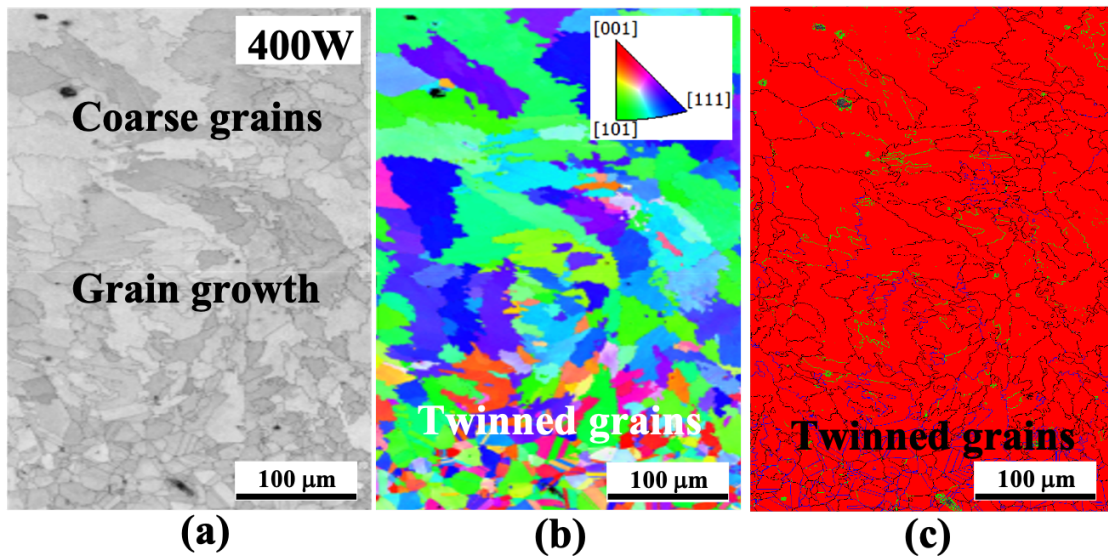
Fig. 4.13 EBSD mappings of the IN625 after laser surface melting at a scanning speed of 800 mm/min with laser power of 400 W. Figures from left to right are band contrast image (a), inversed pole figure (IPF) (b) and phase mapping (c).
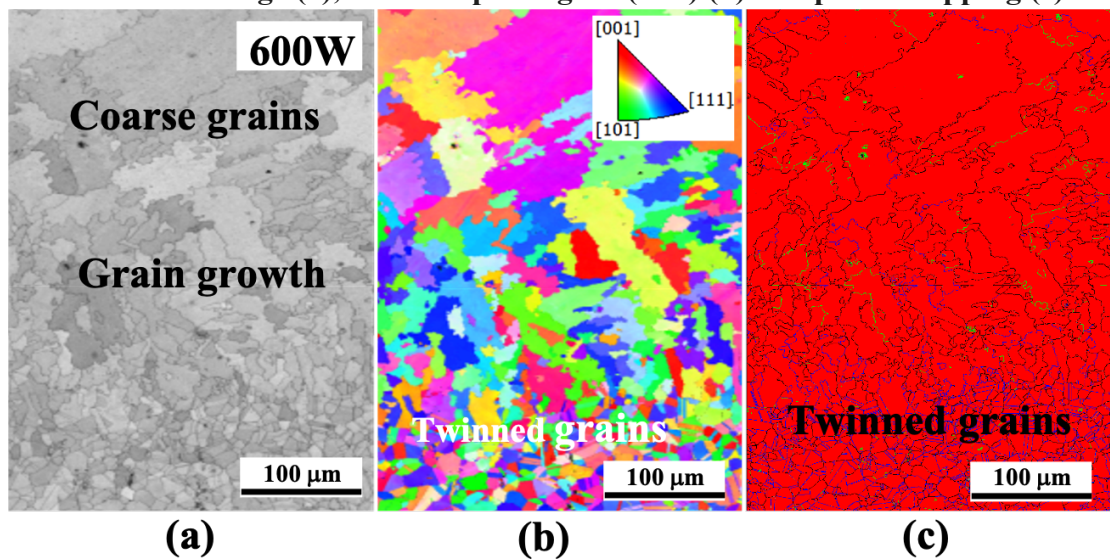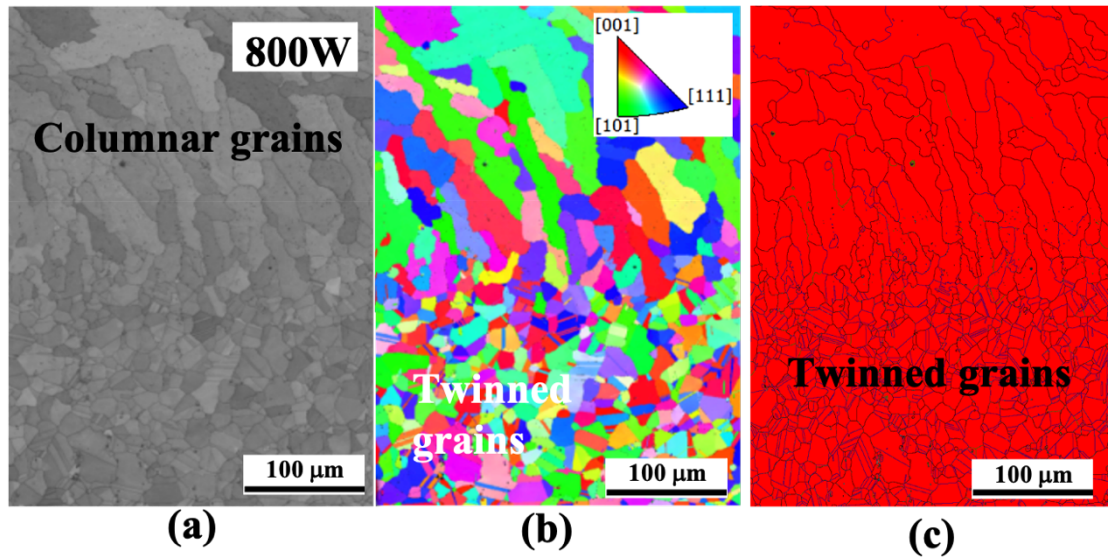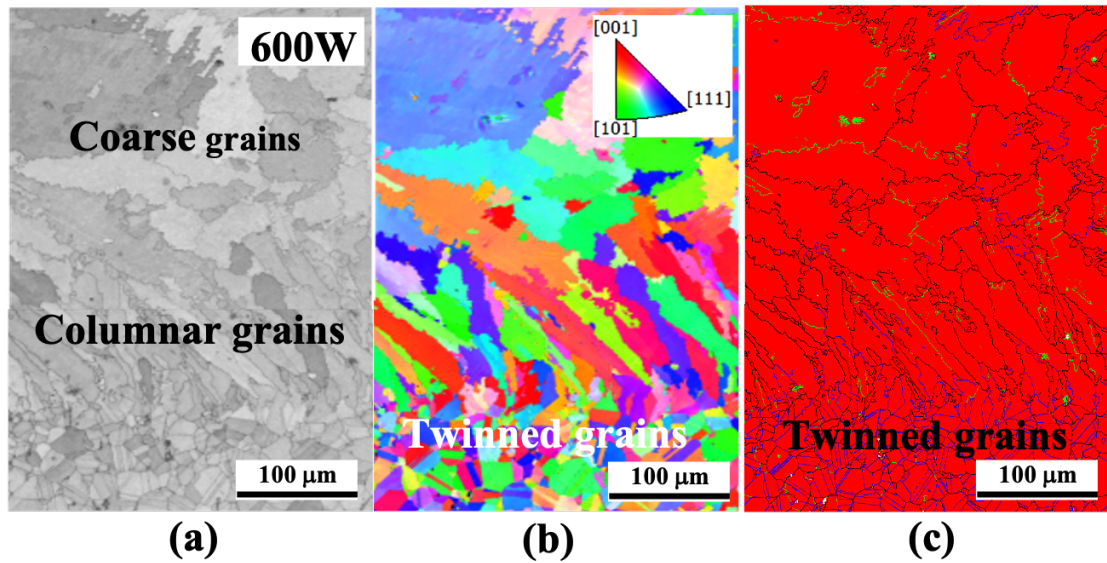
Fig. 4.14 EBSD mappings of the IN625 after laser surface melting at a scanning speed of 800 mm/min with laser power of 600 W. Figures from left to right are band contrast image (a), inversed pole figure (IPF) (b) and phase mapping (c).
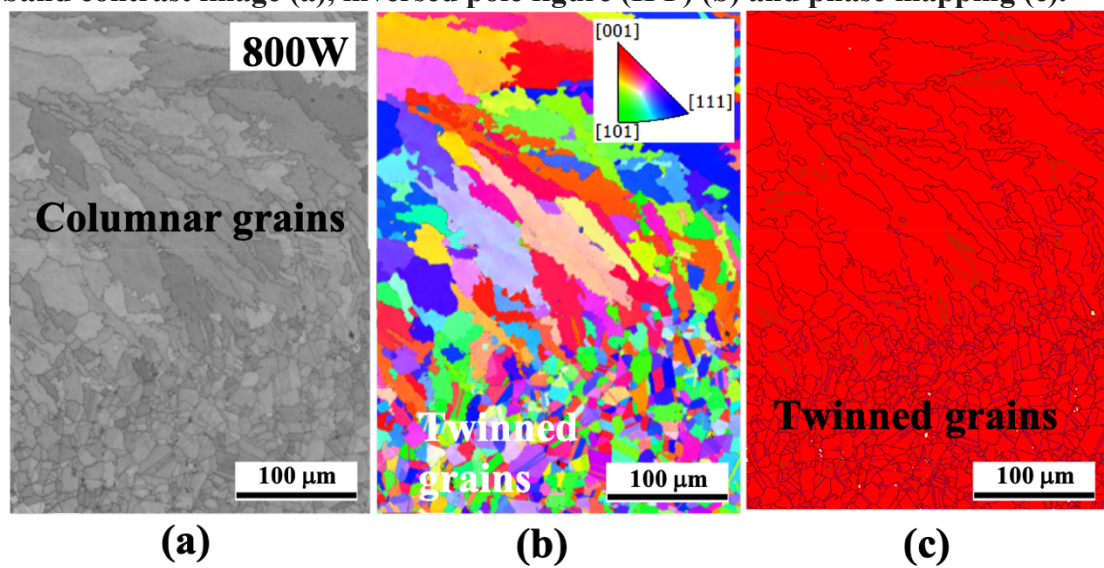
Fig. 4.15 EBSD mappings of the IN625 after laser surface melting at a scanning speed of 800 mm/min with laser power of 800 W. Figures from left to right are band contrast image (a), inversed pole figure (IPF) (b) and phase mapping (c).
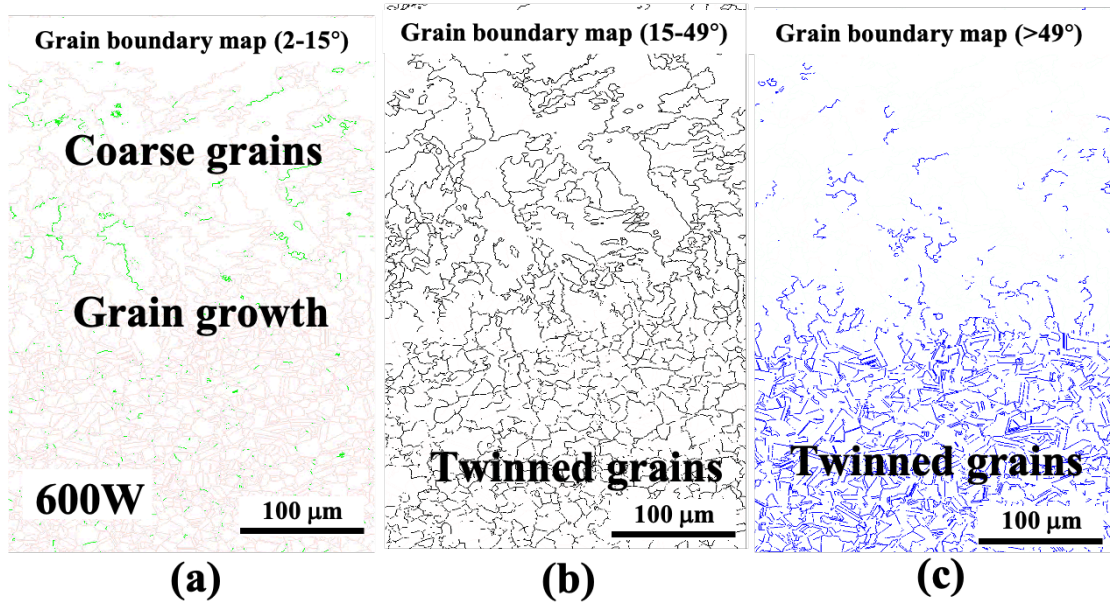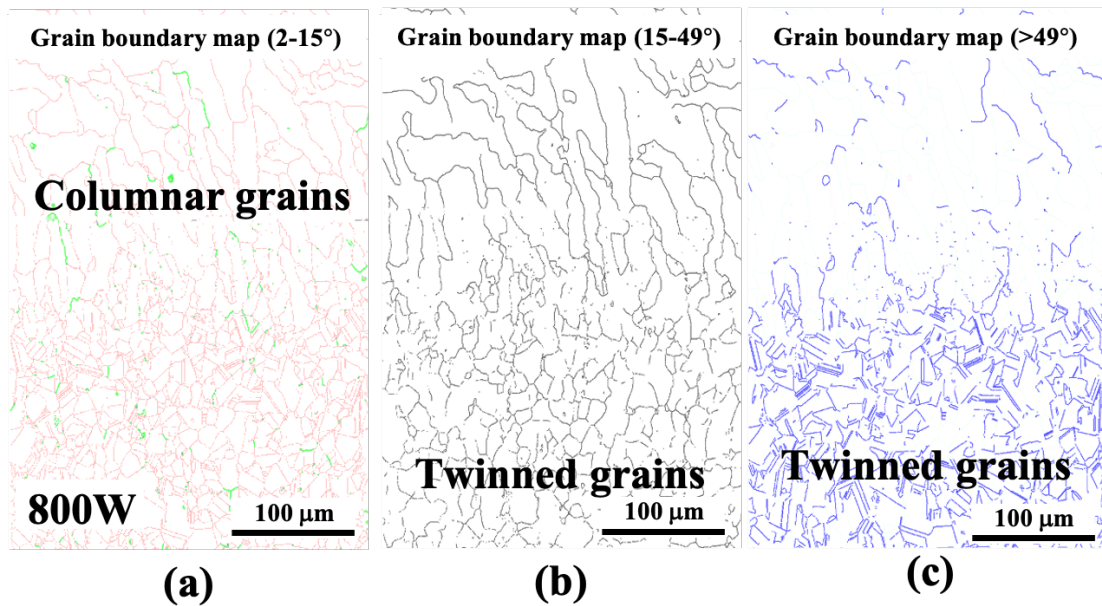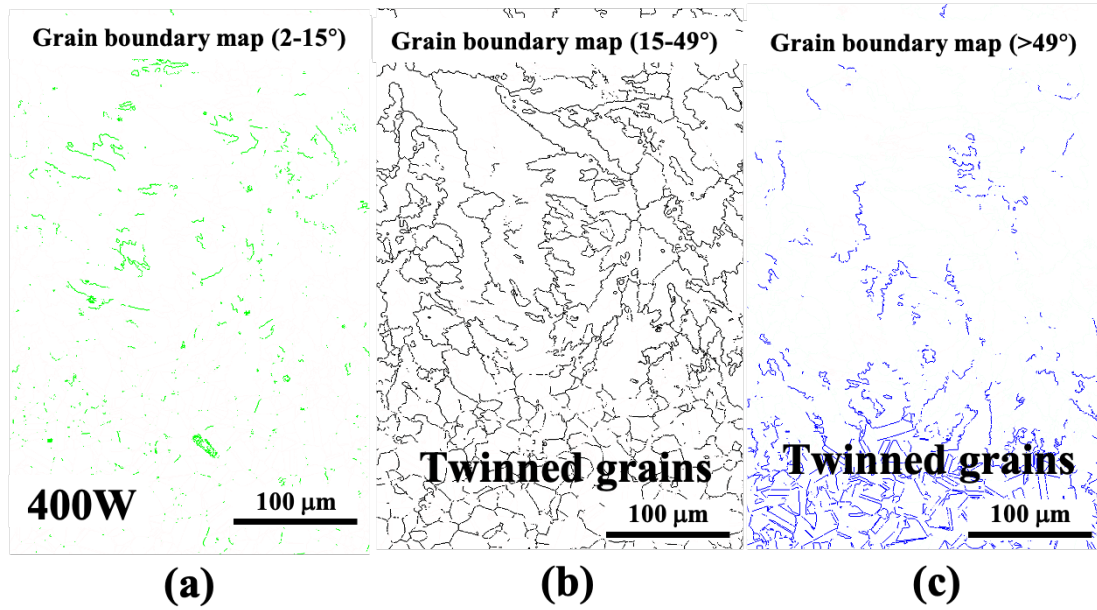
Fig. 4.16 Grain boundary mapping a scanning speed of 800 mm/min with laser power of 400 W. Figures from left to right are grain boundary maps at misorientations <15° (a), 15–49° (b) and >49° (c).
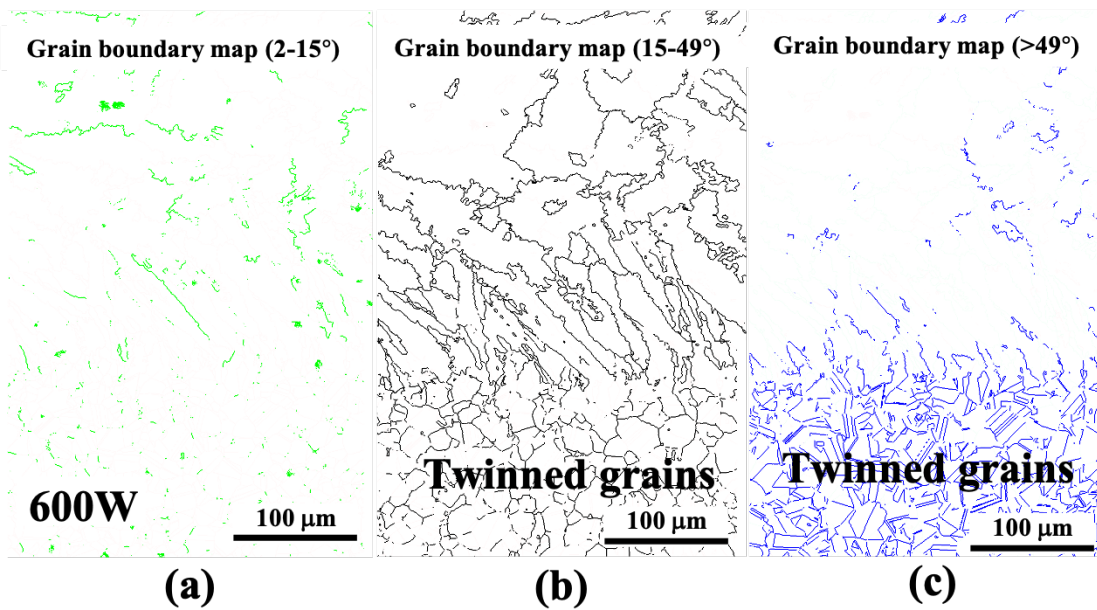
Fig. 4.17 Grain boundary mapping a scanning speed of 800 mm/min with laser power of 600 W. Figures from left to right are grain boundary maps at misorientations <15° (a), 15–49° (b) and >49° (c).
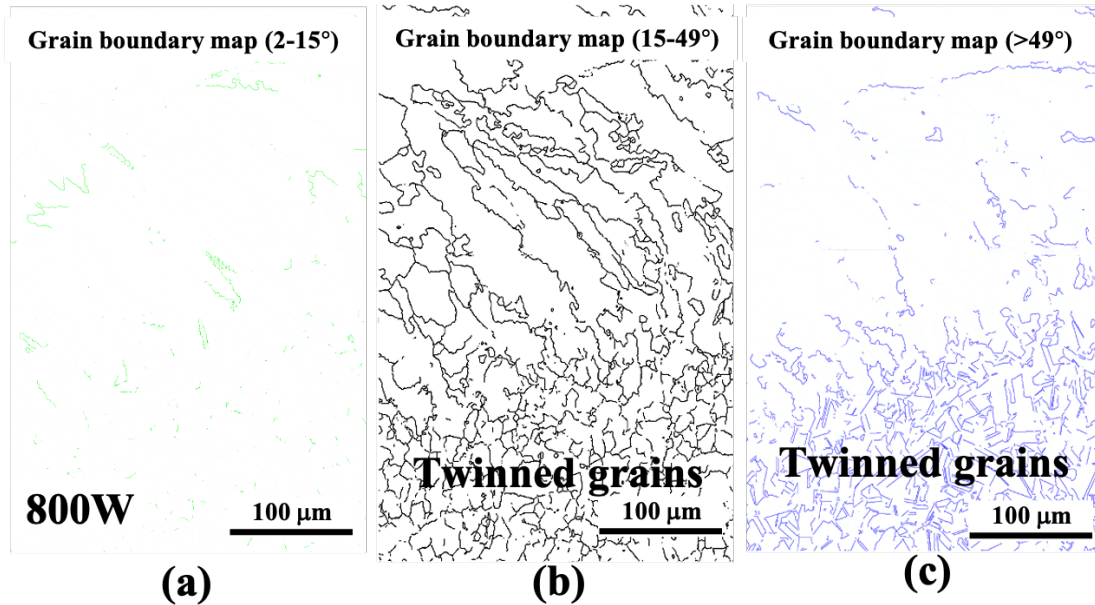
Fig. 4.18 Grain boundary mapping a scanning speed of 800 mm/min with laser power of 800 W. Figures from left to right are grain boundary maps at misorientations <15° (a), 15–49° (b) and >49° (c).

When comparing **Fig. 4.10 - Fig. 4.12** and **Fig. 4.16 - Fig. 4.18**,, the only difference is the scanning speed. It is understood that the energy density decreases with scanning speeds when the laser power is the same. At the laser power of 400 W, the limited energy inputs results in a small melt pool size. The rapid solidification of the small melt pool limits the growth of columnar grains. When the power increases, the columnar grains have time to form within the melt pool due to the increase in the volume of the melt pool with laser power [63]. This is indeed seen in the grain structure of columnar grains at 600 W and 800 W in **Fig. 4.10 - Fig. 4.12** and **Fig. 4.16 - Fig. 4.18**. Since the energy density decreases with scanning speed, the columnar grains are narrower in **Fig. 4.10 - Fig. 4.12** and **Fig. 4.16 - Fig. 4.18**, compared to that in **Fig. 4.9**a. It is because the reduced energy densities at 800 mm/min result in smaller melt pool depth and subsequently restrict the growth of columnar grains. This is evidenced when large columnar grains are seen in **Fig. 4.9**a and **Fig. 4.9**b, in comparison to the narrow

57

columnar grains in **Fig. 4.15**a and **Fig. 4.15**b. Since the energy density is determined by the laser power and scanning speed which in turn governs the melt pool depth, it is important to evaluate the melt pool depth evolution for a better control on the resultant microstructure.

4.6 Melt pool depth calculation

The temperature distribution across the laser melted zone is crucial to evaluate the melt pool depth during laser surface melting at various laser powers and scanning speeds. An analytical approach to estimating the temperature distribution in the welding process was reported by Rosenthal [46] back in the 1940s, which exhibits good similarity to laser surface melting. These semi-quantitative solutions were further extended by Ashby and Esterling to approximate the heat flow after laser surface treatment [47]. For a laser beam moving along the y-axis according to **Fig. 3.2** with a Gaussian energy distribution, the temperature distribution of the melt pool below the centre of laser track for x = 0 is expressed in Eq. (4.1) [67],

$$T(z,t) = T_0 + \frac{AP}{2\pi\lambda v\sqrt{[t(t+t_0)]}} \times \exp\left[-\left(\frac{(z+z_0)^2}{4\alpha t}\right)\right] \qquad (4.1)$$

Where $T(z, t)$ is the temperature below the center of laser track at the depth z and T_0 is the initial ambient temperature, all in K. A is the absorptivity at the sample surface, taken as 0.5 which was quoted in previous studies [68]. P is the laser power (W), λ is the thermal conductivity (W/m/K), is the laser scanning speed (m/s), t is the interaction time (s), t_0 is the time constant (s), z is the depth below the center of the laser track (m), z_0 is the depth constant (m), α is the material thermal diffusivity (m^2/s).

The interaction time t is defined as a ratio of the laser beam radius to the scanning speed, given in Eq. (4.2) [69], where r is the radius of the laser beam, taken as 250 μm, half of the laser bean diameter.

$$t = \frac{2r}{v} \tag{4.2}$$

The time constant is defined as the time required for heat diffusion over a distance equal to the laser beam radius, which is described in Eq. (4.3) [67].

$$t_0 = \frac{r^2}{4\alpha} \tag{4.3}$$

The thermal diffusivity α can be obtained from Eq. (4.4) [70] where λ is the thermal conductivity (W/m/K), ρ is the density (kg/m³) and Cp is the specific heat of the material (J/kg/K).

$$\alpha = \frac{\lambda}{\rho C_p} \tag{4.4}$$

The thermal properties of IN625 used for calculating the thermal diffusivity are summarised in **Table 4.4 [71]**. Since the temperature at the center of the laser spot is well above the melting point of the alloy, the temperature dependent density, thermal conductivity and specific heat in the liquid state of IN625 according to **Table 4.4** are used to estimate the maximum melt pool depth.

Table 4.4 Thermal properties of IN625 used in calculation [71].

Material property	Value
Liquidus temperature, T_L (K)	1623
Solidus temperature, T_S (K)	1563
Density, ρ (kg/m³)	8631.4-0.4467T (for T< T_S) 9143.2-0.9117T (for T> T_L)
Thermal conductivity, λ (W/m/k)	6.1755+0.0161T (for T< T_S) 5.0000+0.0147T for (T> T_L)
Specific heat, C_p (J/kg/K)	312.93+0.2386T (for T< T_S) 704.83+0.0183 (for T> T_L)

The depth constant corresponds to the distance from the surface over which heat diffuses during the interaction time of the laser beam. Depending on the relation between interaction time t and time constant, the depth constant can be calculated as follows [67], where e is the base of natural logarithms:

$$z_0^2 = \frac{r}{e}\sqrt{\frac{\pi \alpha r}{v}}, \qquad (t \gg t_0) \tag{4.5}$$

$$z_0^2 = \frac{\pi \alpha r}{2ev}, \qquad (t \ll t_0) \tag{4.6}$$

Based on the parameters given above, it is found that the interaction time t is much larger than the time constant, even at the highest scanning speed of 800 mm/min. Thus, Eq. (4.5) is used to calculate the depth constant z_0. By combining the above equations into Eq. (4.3), the temperature distribution along the depth of the melt pool is plotted in **Fig. 4.19** at laser power of 400 W, 600 W and 800 W. At 400 W in **Fig. 4.19**a, the peak temperature in the melt pool is about 2500 K, and then gradually decreases with the distance from the surface. At 600 W in **Fig. 4.19**b, the peak temperature at the melt pool surface reaches about 3500 K. This extremely high temperature produces a large

melt pool depth. Considering that the cooling conditions for all the materials are identical, the solidification time increases with the laser power. This allows the coarse grains to form at the melt pool surface and columnar grains to grow inside the melt pool, as indeed seen in **Fig. 4.7 - Fig. 4.9**; **Fig. 4.13 - Fig. 4.15**. Similarly, at a power of 800 W in **Fig. 4.19**c, the peak temperature goes above 4500 K, resulting in much larger melt pool depths.
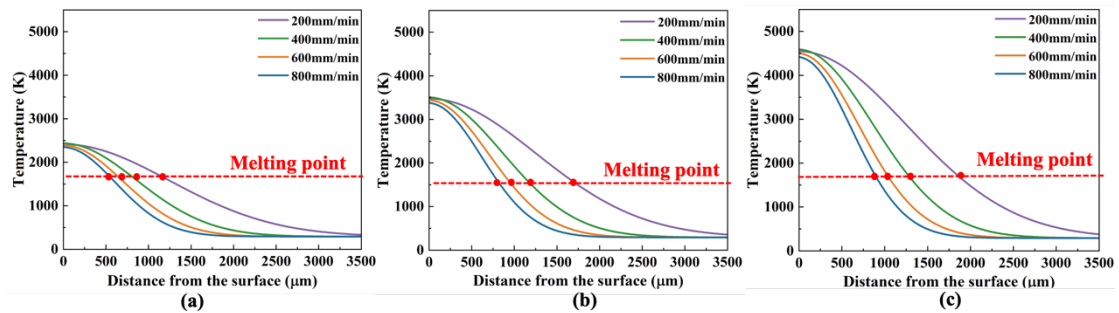
Fig. 4.19. Plot of temperature against distance from the surface to the base material in XZ plane using Eq. (3) at the laser power of 400 W (a), 600 W (b) and 800 W (c).

4.7   Melt pool depth evolution

The experimentally measured melt pool depths at different laser powers and scanning speeds are summarised in **Fig. 4.20**, in comparison to the calculated melt pool depths from **Fig. 4.19**. It can be seen that the experimentally measured melt pool depth increases with laser power and decreases with scanning speed. At a low laser power of 400 W, the melt pool depth decreases slowly with the scanning speed, from 0.8 to 0.4 mm when the scanning speeds increases from 200 to 800 mm/min. The calculated melt pool depths are slightly larger than experimental measurements, from 1.3 to 0.6 mm. A better agreement between experimental and calculated melt pool depth is achieved at a laser power of 600 W, from 1.6 mm to 0.9 mm when the scanning speed increases,

showing the reliability of the above analytical solutions in predicting the melt pool depth during laser surface melting. But at high laser power of 800 W, the experimental melt pool depths are quite large and fluctuate with scanning speeds, ranging from 2.6 to 1.9 mm, whilst the calculated melt pool depths are from 2.3 to 1.2 mm. It should also be noted that the experimentally measured melt pool depths at 800 W are prone to scattering. This is because the large laser power at 800 W provides a very high energy density that melts the material and produces a large melt pool depth. The high energy density generates surface morphology changes due to the fluid flow in the melt pool [69], and subsequently causes the development of non-uniform melt pool boundaries. The higher the laser power, the deeper the melt depth. A deeper melt depth was found with a lower scan speed when laser power is fixed. It could be explained by the heat input to melt pool. When laser power is higher or the scan speed is lower, which means the heat input by the laser per unit time in a unit length is higher, and thus a deeper melt depth was formed. **Fig. 4.21** shows the surface roughness measurements after laser surface melting. It can be seen clearly that high Ra values are resulted at 800 W, indicating strong melt pool instability at high laser power. Similar findings have also been reported in the literature, especially at high laser powers. Investigations using pulsed lasers have reported that top surface roughness can be reduced using a low scan speed and high repetition rate due to melt pool stabilization and reduced surface profile variation on top of the solidified melt pool [72, 73]. Liu et al. reported that the melt pool depths were underestimated at high energy densities [74]. However, low scan speeds can significantly increase the volume of melt pool produced and promote a

phenomenon known as balling. Balling is the breakup of the melt pool into small spheres. It occurs when molten material does not wet well to the underlying substrate or material due to high surface tension differences generated as a result of variations in thermal properties within the melt pool [75-77]. These thermal gradients cause a thermocapillary flow of a fluid within the melt pool from regions with low surface tension to regions with high surface tension, known as Marangoni convection [78] It is widely recognised that a keyhole melt pool morphology with a narrow melt pool width and large melt pool depth is often obtained under high laser power [79]. The intense recoil pressure broadens the melt pool width, and deepens the melt pool bottom greatly, forming a keyhole. The simplified analytical solution to the melt pool depth may fail to describe these effects sufficiently. Besides, underestimating laser absorptivity at high energy and neglecting the effect of the plasma plume at high temperatures may also be the cause of the error.
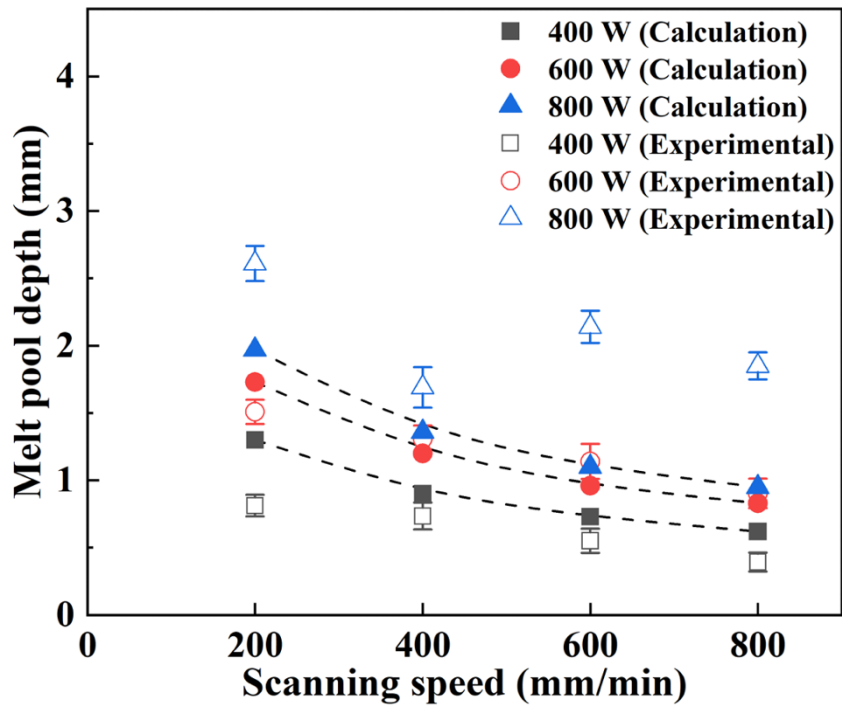
Fig. 4.20 The comparison between experimentally measured and mathematically calculated melt pool depth against scanning speeds at laser power of 400 W, 600 W and 800 W. The error bar represents the standard deviation of the melt pool depth measurements.
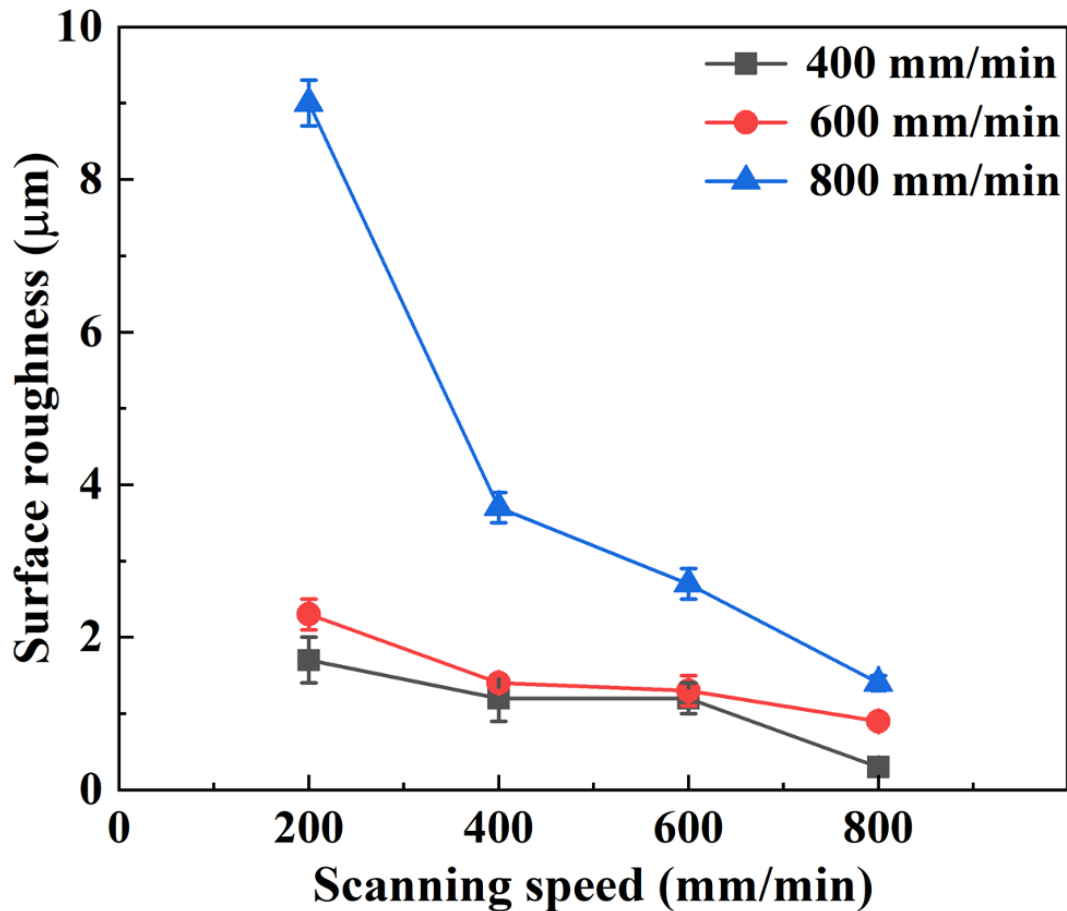
Fig. 4.21 The comparison of the surface roughness Ra after laser surface melting, showing that high surface roughness is resulted at 800 W.

To evaluate the resultant microstructural changes on the mechanical properties of IN625 after laser surface melting, the hardness profiles from the surface to the base material is depicted in **Fig. 4.22**. It can be seen from **Fig. 4.22**a that the hardness near the surface increases with scanning speeds at 400 W. It was previously seen from **Fig. 4.20** that the melt pool depth decreases with scanning speed. That means more rapid cooling and solidification occurs when the scanning speed increases, which may limit the grain growth and enhance the surface hardness. **Fig. 4.22**a and **Fig. 4.22**c also suggests that the hardness near the surface increases with scanning speed. Similar finding has also been reported by Bera et al., in which the hardness was shown to increase with the scanning speed [38]. It is noted that the hardness values near the

surface at 800 W in **Fig. 4.22**c are slightly smaller than those in **Fig. 4.22**a and **Fig. 4.22**b. This is because the large laser power (800 W) results in significant grain growth. It is evidenced from **Fig. 4.7** -**Fig. 4.9**; **Fig. 4.13** - **Fig. 4.15**, that coarse grains and columnar grains are formed when the laser power increases. These coarse grains that form at high laser power reduce the surface hardness of the material. Given that the melt pool depth at 800 W is significantly larger than that at 400 W and 600 W, as shown in **Fig. 4.20**, the hardness in the melt pool is smaller due to the grain growth behaviour at large power inputs.
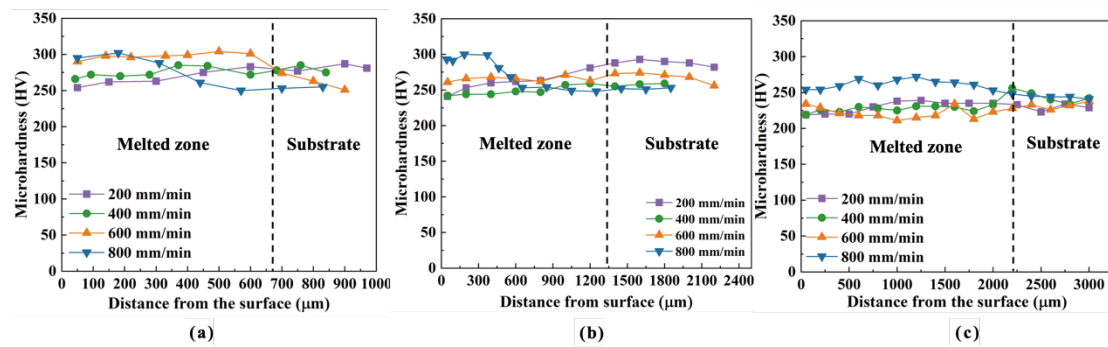
Fig. 4.22 The microhardness measurements from the surface to the base material for laser power of 400 W (a), 600 W (b) and 800 W (c) at scanning speeds from 200 mm/min to 800 mm/min.

It is also widely acknowledged that laser surface melting can refine the grain size at the surface [80]. But this usually occurs in pulsed or picosecond/femtosecond laser surface treatments which have a very high cooling rate of 5×10^6 K/s and shallow melt pool depth [81]. However, the continuous laser mode, especially at high laser power, generates excessive heat input and surface melting. This is seen in **Fig. 4.20**, where the melt pool depth increases to almost 2.5 mm at 800 W. The large melt pool without effective cooling allows grains to grow during solidification, which is similar to that in the laser welding process [82]. Given that the volume of the samples (20 mm in

diameter and 10 mm in thickness) is quite small, the heat dissipation is quite limited. Besides, an overlap ratio of 50 % during laser surface melting causes further heat accumulation, allowing the grains to grow within the melt pool. Thus, coarse grains and columnar grains are formed, as observed from **Fig. 4.7** - **Fig. 4.9**; **Fig. 4.13** - **Fig. 4.15**. A schematic diagram for the above grain growth behaviour is illustrated in **Fig. 4.23**. **Fig. 4.23**a is the as-cast equiaxed grain structure before laser surface melting is carried out, during the laser surface melting process, melting occurs from the upper surface, forming a solid-liquid coexistence, as shown in **Fig. 4.23**b. **Fig. 4.23**c - **Fig. 4.23**d is the stage of upward growth of the grains, which are formed as equiaxed columnar crystals at the boundary of the molten pool, and coarse grains are formed close to the surface.

(a)

(b)

(c)

(d)
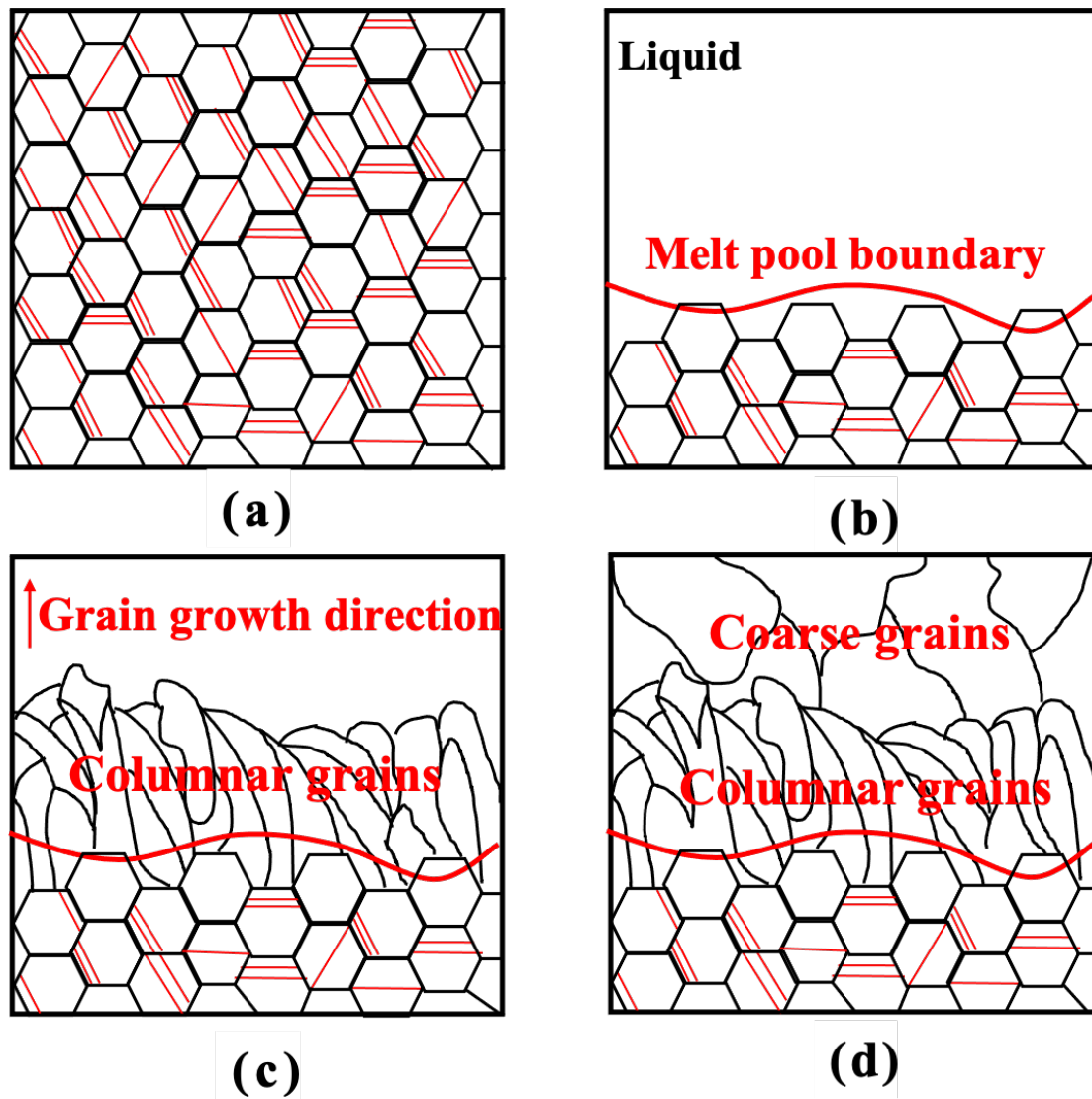
Fig. 4.23 A schematic diagram to illustrate the grain growth behaviour: As-cast equiaxed grain structure (a), laser surface melt pool (b), columnar grain growth stage from the melt pool boundary (c), coarse grain growth stage at the top of the melt pool (d).

Chapter 5 Conclusion

In this study, the microstructural evolution and grain structure characteristics of IN625 were investigated after laser surface melting at laser powers from 400 W to 800 W and scanning speeds ranging from 200 mm/min to 800 mm/min. The effects of laser power and scanning speeds on the cellular structure formation and grain growth behaviour were discussed. An analytical approach was employed to calculate the temperature distribution across the melt pool. The main conclusions were drawn as follows:

- The laser surface melting caused heavy element segregation, resulting in the secondary phase forming within the γ matrix of IN625. It was found that the cellular structure was able to form when the energy density was ≤ 240 J/mm^2. This was likely due to the fact that low energy densities caused rapid heating and cooling, allowing cellular structures to form during laser surface melting.

- Large angle grain boundaries were eliminated in the melt pool after laser surface melting. This was because sufficient melting allowed the initial twinned grains of IN625 to be fully melted, and no twinned grains could form in the grain growth stage. No preferred grain orientations were developed due to the relatively rapid heating and solidification in laser surface melting.

- Good agreement between the experimentally measured and mathematically calculated melt pool depths was achieved at a laser power of 400 W and 600 W. Some discrepancies were noticed at 800 W, which was likely caused by the high heat input and instability of melt flow dynamics in the melt pool.

Overall, this study presents a systematic investigation of the microstructural changes and grain growth characteristics of IN625 after laser surface melting. An appropriate range of energy density is required to achieve a refined cellular structure. Moreover, grain growth occurs at the melt pool boundaries, forming columnar grains within the melt pool and coarse grains near the surface. A surface hardening effect, especially at high scanning speed (i.e. 800 mm/min), is also noticed after laser surface melting. This hardening effect is quite limited due to the large grain size across the melt pool. It is further revealed that large angle grain boundaries are eliminated during the laser surface melting process, which is attributed to the sufficient melting of twinned grains. The findings in the study are believed to be helpful in designing graded structures by carefully controlling the laser power and scanning speed. Future work on characterisation of wear and corrosion performance is necessary to establish the structure-process-performance interrelationship in laser surface melting.

Chapter 6 Future work

This work focuses on the evolution of the microstructure and grain properties of the IN625 alloy at different powers and scanning speeds, in this study, it was found that grain growth occurs at the melt pool boundary, forming columnar grains in the melt pool and coarse grains on the surface. It was also found that the honeycomb phase structure is formed only at a low energy density. However, there are some limitations to this work that could be further improved in future work, and these are as follows.

- IN625 undergoes laser surface melting and experiences phase transformations, we are interested in what new changes will occur to IN625 under conditions of high-temperature oxidation. Conduct high-temperature oxidation resistance tests on IN625 alloy after laser surface melting to analyse at which process parameters the oxidation resistance is better.

- After LSM, the grain boundary angles will change. We know that variations in grain boundary angles affect the mechanical properties of the material, so we are prepared to conduct tensile tests. tensile properties make the response of the material to withstand tensile force, and explore the effect of LSM on the tensile properties of the material through relevant tests.

- Coarse grains are produced by LSM, and different grain sizes have different effects on the uniformity of the reinforcing phase distribution, leading to changes in the wear resistance of the material. Therefore, we will conduct wear tests to further determine the impact of LSM on the material's wear resistance.

- LSM refines the microstructure and affects the grain size. Changes in grain size can impact the material's corrosion resistance, so we are preparing to conduct corrosion resistance tests, and the effect of LSM on corrosion resistance was investigated by immersing the samples in corrosive solutions to simulate artificial corrosion and observing the corrosion resistance of the alloys.

References

[1] S. Masood Arif Bukhari, N. Husnain, F. Arsalan Siddiqui, M. Tuoqeer Anwar, A. Abbas Khosa, M. Imran, T. Hassan Qureshi, R. Ahmad, Effect of laser surface remelting on Microstructure, mechanical properties and tribological properties of metals and alloys: A review, Optics & Laser Technology 165 (2023) 109588.

[2] S. Sarkar, C.S. Kumar, A.K. Nath, Effects of different surface modifications on the fatigue life of selective laser melted 15–5 PH stainless steel, Materials Science and Engineering: A 762 (2019) 138109.

[3] M.R. Mahbub, A. Rashid, M.P. Jahan, Hybrid machining and finishing processes, Advanced Machining and Finishing 2021, pp. 287-338.

[4] J. Wu, J. Yu, W. Wang, S. Gao, J. Luo, C. Li, Z. Ma, Y. Liu, Influences of laser remelting treatments on microstructure and tensile properties of multiphase Ni3Al-based intermetallic alloy, Materials Science and Engineering: A 857 (2022) 144087.

[5] B. Mojškerc, D. Ravnikar, R. Šturm, Experimental characterisation of laser surface remelting via acoustic emission wavelet decomposition, Journal of Materials Research and Technology 15 (2021) 3365-3374.

[6] C. Zhang, L. Chai, Y. Liu, Z. Li, F. Zhang, X. Li, Z. Fu, Correlating microstructural features with improved wear and corrosion resistance of laser surface remelted A356 alloy at different scanning speeds, Materials Characterization 202 (2023) 113021.

[7] J.K. Chaurasia, A.N. Jinoop, P. P, C.P. Paul, K.S. Bindra, S. Bontha, Study of melt pool geometry and solidification microstructure during laser surface melting of Inconel 625 alloy, Optik 246 (2021) 167766.

[8] J. Kusinski, S. Kac, A. Kopia, A. Radziszewska, M. Rozmus-Górnikowska, B. Major, L. Major, J. Marczak, A. Lisiecki, Laser modification of the materials surface layer-a review paper, Bulletin of the Polish Academy of Sciences: Technical Sciences 60(4) (2012) 711-728.

[9] L. Gomell, S.-P. Tsai, M. Roscher, R. Bueno Villoro, P. Konijnenberg, S. Zaefferer, C. Scheu, B. Gault, In situ nitriding of Fe 2 VAl during laser surface remelting to manipulate microstructure and crystalline defects, Physical Review Materials 6(8) (2022) 085405.

[10] P. Dinesh Babu, K. Balasubramanian, G. Buvanashekaran, Laser surface hardening: a review, International Journal of Surface Science and Engineering 5(2-3) (2011) 131-151.

[11] S.M.A. Bukhari, N. Husnain, F.A. Siddiqui, M.T. Anwar, A.A. Khosa, M. Imran, T.H. Qureshi, R. Ahmad, Effect of laser surface remelting on Microstructure, mechanical properties and tribological properties of metals and alloys: A review, Optics & Laser Technology 165 (2023) 109588.

[12] N. Ahmadi, H. Naffakh-Moosavy, S.M.M. Hadavi, F. Bagheri, The effect of Nd:YAG laser parameters on the microstructure, hot cracking susceptibility and elemental evaporation of surface melted AZ80 magnesium-based alloy, Journal of Materials Research and Technology 27 (2023) 2459-2474.

[13] K.Y. Benyounis, O.M.A. Fakron, J.H. Abboud, A.G. Olabi, M.J.S. Hashmi, Surface melting of nodular cast iron by Nd-YAG laser and TIG, Journal of Materials Processing Technology 170(1) (2005) 127-132.

[14] Y. Yu, M. Zhang, Y. Guan, P. Wu, X. Chong, Y. Li, Z. Tan, The effects of laser remelting on the microstructure and performance of bainitic steel, Metals 9(8) (2019) 912.

[15] C. Wang, H. Zhou, Z. Zhang, Y. Zhao, P. Zhang, D. Cong, C. Meng, F. Tan, Tensile property of a hot work tool steel prepared by biomimetic coupled laser remelting process with different laser input energies, Applied surface science 258(22) (2012) 8732-8738.

[16] B.V. Krishna, A. Bandyopadhyay, Surface modification of AISI 410 stainless steel using laser engineered net shaping (LENSTM), Materials & Design 30(5) (2009) 1490-1496.

[17] J. Ghorbani, J. Li, A.K. Srivastava, Application of optimized laser surface re-melting process on selective laser melted 316L stainless steel inclined parts, Journal of Manufacturing Processes 56 (2020) 726-734.

[18] Z. Hu, B. Nagarajan, X. Song, R. Huang, W. Zhai, J. Wei, Tailoring surface roughness of micro selective laser melted SS316L by in-situ laser remelting, Advanced Surface Enhancement: Proceedings of the 1st International Conference on Advanced Surface Enhancement (INCASE 2019)—Research Towards Industrialisation, Springer, 2020, pp. 337-343.

[19] J. Sušnik, R. Šturm, J. Grum, Influence of laser surface remelting on Al-Si alloy properties, Strojniški vestnik-Journal of Mechanical Engineering 58(10) (2012) 614-620.

[20] Q. Qin, G.X. Chen, Effects of parameters on surface roughness of metal parts by

selective laser melting, Advanced Materials Research 834 (2014) 872-875.

[21] R. Shoja-Razavi, Laser surface treatment of stellite 6 coating deposited by HVOF on 316L alloy, Journal of Materials Engineering and Performance 25 (2016) 2583-2595.

[22] C.-R. CIUBOTARIU, V.-A. SERBAN, G. MARGINEAN, D. FRUNZAVERDE, New Structural and Morphological Properties of Thermally Sprayed Stellite Coatings After Laser Remelting, Proceeding of International Conference of Metal, Brno, Czech Republic, 2012.

[23] C.-R. Ciubotariu, D. Frunzăverde, G. Mărginean, V.-A. Șerban, A.-V. Bîrdeanu, Optimization of the laser remelting process for HVOF-sprayed Stellite 6 wear resistant coatings, Optics & Laser Technology 77 (2016) 98-103.

[24] B. Norhafzan, S. Aqida, C. Khairil, Optimization of laser melting parameter to enhanced surface properties in hot press forming die, IOP Conference Series: Materials Science and Engineering, IOP Publishing, 2021, p. 012020.

[25] Y. Chen, X. Li, J. Liu, Y. Zhang, X. Chen, Effect of scanning speed on properties of laser surface remelted 304 stainless steel, Micromachines 13(9) (2022) 1426.

[26] K.C. Vidyasagar, A. Rana, D. Kalyanasundaram, Optimization of laser parameters for improved corrosion resistance of nitinol, Materials and Manufacturing Processes 35(14) (2020) 1661-1669.

[27] J. Zhang, M. Yu, Z. Li, Y. Liu, Q. Zhang, R. Jiang, S. Sun, The effect of laser energy density on the microstructure, residual stress and phase composition of H13 steel treated by laser surface melting, Journal of Alloys and Compounds 856 (2021) 158168.

[28] Q. Shi, D. Gu, M. Xia, S. Cao, T. Rong, Effects of laser processing parameters on

thermal behavior and melting/solidification mechanism during selective laser melting of TiC/Inconel 718 composites, Optics & Laser Technology 84 (2016) 9-22.

[29] B. Zhang, H. Liao, C. Coddet, Effects of processing parameters on properties of selective laser melting Mg–9% Al powder mixture, Materials & Design 34 (2012) 753-758.

[30] E. Yasa, J. Deckers, J.P. Kruth, The investigation of the influence of laser re-melting on density, surface quality and microstructure of selective laser melting parts, Rapid Prototyping Journal 17(5) (2011) 312-327.

[31] A.K. Praharaj, J.K. Chaurasia, G.R. Chandan, S. Bontha, P.S. Suvin, Enhanced tribological performance of laser directed energy deposited Inconel 625 achieved through laser surface remelting, Surface and Coatings Technology 477 (2024) 130345.

[32] M. Skalon, B. Meier, T. Leitner, S. Arneitz, S.T. Amancio-Filho, C. Sommitsch, Reuse of Ti6al4V powder and its impact on surface tension, melt pool behavior and mechanical properties of additively manufactured components, Materials 14(5) (2021) 1251.

[33] X. Yan, S. Gao, C. Chang, J. Huang, K. Khanlari, D. Dong, W. Ma, N. Fenineche, H. Liao, M. Liu, Effect of building directions on the surface roughness, microstructure, and tribological properties of selective laser melted Inconel 625, Journal of Materials Processing Technology 288 (2021) 116878.

[34] S. Das, Physical Aspects of Process Control in Selective Laser Sintering of Metals, Advanced Engineering Materials 5(10) (2003) 701-711.

[35] C. Palanisamy, R. Raman, P.A. Olubambi, Microstructural characteristics,

hardness and tribological behavior of additive manufactured CM247LC nickel super alloy, Engineering Headway 4 (2024) 3-14.

[36] D. Wang, Y. Liu, Y. Yang, D. Xiao, Theoretical and experimental study on surface roughness of 316L stainless steel metal parts obtained through selective laser melting, Rapid Prototyping Journal 22(4) (2016) 706-716.

[37] J. Vaithilingam, R.D. Goodridge, R.J.M. Hague, S.D.R. Christie, S. Edmondson, The effect of laser remelting on the surface chemistry of Ti6al4V components fabricated by selective laser melting, Journal of Materials Processing Technology 232 (2016) 1-8.

[38] T. Bera, I. Manna, J. Dutta Majumdar, Titanium carbide (TiC) dispersed surface on titanium based alloy (Ti-13Nb-13Zr) by in-situ laser composite surfacing and its wear performance, Journal of Materials Processing Technology 328 (2024) 118394.

[39] T. Lee, Variation in mechanical properties of TI-13NB-13ZR depending on annealing temperature, Applied Sciences (Switzerland) 10(21) (2020) 1-7.

[40] Q. Li, F. Guo, L. Chai, Y. Ma, L. Jiang, Q. Chen, C. Zhang, H. Liu, D. Zhang, B. Jiang, Redistribution and refinement of the dendrites in a Mg-Y alloy by laser surface remelting and its influence on mechanical properties, Materials Science and Engineering: A 848 (2022) 143362.

[41] Q. Sun, J. Yang, R. Tian, X. Fan, Z. Liao, M. Zhu, Enhanced corrosion and wear resistances in a precipitate-hardened magnesium alloy by laser surface remelting, Materials Characterization 193 (2022) 112306.

[42] Z. Chong, Y. Sun, W. Cheng, L. Huang, C. Han, X. Ma, A. Meng, Laser remelting induces grain refinement and properties enhancement in high-speed laser cladding

AlCoCrFeNi high-entropy alloy coatings, Intermetallics 150 (2022) 107686.

[43] H. Shiratori, T. Fujieda, K. Yamanaka, Y. Koizumi, K. Kuwabara, T. Kato, A. Chiba, Relationship between the microstructure and mechanical properties of an equiatomic AlCoCrFeNi high-entropy alloy fabricated by selective electron beam melting, Materials Science and Engineering: A 656 (2016) 39-46.

[44] S. Yuan, Z. Gao, H. Fu, C.F. Cheung, X.S. Yang, Superior corrosion-resistant nanostructured hypoeutectic CrCoNi-based medium-entropy alloy processed by laser surface remelting, Journal of Alloys and Compounds 967 (2023) 171802.

[45] J. Dutta Majumdar, R. Galun, B.L. Mordike, I. Manna, Effect of laser surface melting on corrosion and wear resistance of a commercial magnesium alloy, Materials Science and Engineering: A 361(1-2) (2003) 119-129.

[46] D. Rosenthal, Mathematical Theory of Heat Distribution During Welding and Cutting, Welding Journal 20(5) (1941) 220s-234s.

[47] M.F. Ashby, K.E. Easterling, The transformation hardening of steel surfaces by laser beams-I. Hypo-eutectoid steels, Acta Metallurgica 32(11) (1984) 1935-1937,1939.

[48] N. Wang, J. Shen, S. Hu, Y. Liang, Numerical analysis of the TIG arc preheating effect in CMT based cladding of Inconel 625, Engineering Research Express 2(1) (2020) 015030.

[49] R. Andreotta, L. Ladani, W. Brindley, Finite element simulation of laser additive melting and solidification of Inconel 718 with experimentally tested thermal properties, Finite Elements in Analysis and Design 135 (2017) 36-43.

[50] S. Lu, H. Fujii, H. Sugiyama, M. Tanaka, K. Nogi, Effects of Oxygen Additions to

Argon Shielding Gas on GTA Weld Shape, ISIJ International 43(10) (2003) 1590-1595.

[51] H. Yeo, M. Son, H. Ki, Investigation of microstructure and residual stress development during laser surface melting of AH36 steel using 3-D fully coupled numerical model, International Journal of Heat and Mass Transfer 197 (2022) 123366.

[52] W. Jia, S. Chen, L. Zhou, J. Chen, Y. Wang, T. Cui, J. Liang, M. Wang, Influence of energy area densities on microstructure evolution and properties of laser direct energy deposited Ni-Co-Mn-Al-Y magnetic shape memory alloy, Additive Manufacturing 60 (2022) 103232.

[53] E. Chlebus, K. Gruber, B. Kuźnicka, J. Kurzac, T. Kurzynowski, Effect of heat treatment on the microstructure and mechanical properties of Inconel 718 processed by selective laser melting, Materials Science and Engineering: A 639 (2015) 647-655.

[54] J.C. Lourenço, L.P. Souza, M.I.S.T. Faria, C.A. Nunes, C.R. Tomachuk, M.A. Baker, Influence of the iron content on the microstructure and electrochemical behavior of as-cast modified Inconel 625, Corrosion Science 193 (2021) 109892.

[55] N.T. Aboulkhair, M. Simonelli, L. Parry, I. Ashcroft, C. Tuck, R. Hague, 3D printing of Aluminium alloys: Additive Manufacturing of Aluminium alloys using selective laser melting, Progress in Materials Science 106 (2019) 100578.

[56] P. Tao, H. Li, B. Huang, Q. Hu, S. Gong, Q. Xu, The crystal growth, intercellular spacing and microsegregation of selective laser melted Inconel 718 superalloy, Vacuum 159 (2019) 382-390.

[57] A. Jha, S. Shukla, A. Choudhary, R. Manoharan, G. Muvvala, A study on developing process-structure–property relationship with molten pool thermal history

during laser surface remelting of Inconel 718, Optics and Laser Technology 157 (2023) 108732.

[58] T. Antonsson, H. Fredriksson, The effect of cooling rate on the solidification of INCONEL 718, Metallurgical and Materials Transactions B: Process Metallurgy and Materials Processing Science 36(1) (2005) 85-96.

[59] G.P. Dinda, A.K. Dasgupta, J. Mazumder, Laser aided direct metal deposition of Inconel 625 superalloy: Microstructural evolution and thermal stability, Materials Science and Engineering: A 509(1-2) (2009) 98-104.

[60] S. Anishetty, T. Bera, S.K. Karak, J. Dutta Majumdar, I. Manna, Microstructure and Properties of Laser Surface Melted AISI 316L Stainless Steel, Journal of Materials Engineering and Performance (2024) 1-16.

[61] J. Dutta Majumdar, I. Manna, Laser material processing, International Materials Reviews 56(5-6) (2011) 341-388.

[62] G.P. Dinda, A.K. Dasgupta, J. Mazumder, Texture control during laser deposition of nickel-based superalloy, Scripta Materialia 67(5) (2012) 503-506.

[63] I. Yadroitsev, P. Krakhmalev, I. Yadroitsava, S. Johansson, I. Smurov, Energy input effect on morphology and microstructure of selective laser melting single track from metallic powder, Journal of Materials Processing Technology 213(4) (2013) 606-613.

[64] A. Hussein, L. Hao, C. Yan, R. Everson, Finite element simulation of the temperature and stress fields in single layers built without-support in selective laser melting, Materials and Design 52 (2013) 638-647.

[65] L. Thijs, M.L. Montero Sistiaga, R. Wauthle, Q. Xie, J.P. Kruth, J. Van Humbeeck,

Strong morphological and crystallographic texture and resulting yield strength anisotropy in selective laser melted tantalum, Acta Materialia 61(12) (2013) 4657-4668.

[66] D. Dai, D. Gu, Thermal behavior and densification mechanism during selective laser melting of copper matrix composites: Simulation and experiments, Materials and Design 55 (2014) 482-491.

[67] A. Bendoumi, N. Makuch, R. Chegroune, M. Kulka, M. Keddam, P. Dziarski, D. Przestacki, The effect of temperature distribution and cooling rate on microstructure and microhardness of laser re-melted and laser-borided carbon steels with various carbon concentrations, Surface and Coatings Technology 387 (2020) 125541.

[68] S. Ghosh, L. Ma, L.E. Levine, R.E. Ricker, M.R. Stoudt, J.C. Heigel, J.E. Guyer, Single-Track Melt-Pool Measurements and Microstructures in Inconel 625, JOM 70(6) (2018) 1011-1016.

[69] J. Xu, P. Zou, L. Liu, W. Wang, D. Kang, Investigation on the mechanism of a new laser surface structuring by laser remelting, Surface and Coatings Technology 443 (2022) 128615.

[70] H. Chen, L. Li, R. Yang, W. Zhu, A. Rushworth, Y. Yin, X. Wang, Microstructure and thermophysical properties of as-cast CoNiCrAl bond coat alloys at different Al contents, Journal of Alloys and Compounds 918 (2022) 165575.

[71] M. Abdelmoula, W. Musinski, Predicting and correlating melt pool characteristics with processing parameters in IN625 powder bed fusion additive manufacturing, Journal of Manufacturing Processes 121 (2024) 427-445.

[72] H.J. Niu, I.T.H. Chang, Liquid phase sintering of M3/2 high speed steel by

selective laser sintering, Scripta Materialia 39(1) (1998) 67-72.

[73] J. Ramos, D. Bourell, J. Beaman, Surface over-melt during laser polishing of indirect-SLS metal parts, MRS Online Proceedings Library (OPL) 758 (2002) LL1. 9.

[74] B. Liu, G. Fang, L. Lei, An analytical model for rapid predicting molten pool geometry of selective laser melting (SLM), Applied Mathematical Modelling 92 (2021) 505-524.

[75] J.P. Kruth, L. Froyen, J. Van Vaerenbergh, P. Mercelis, M. Rombouts, B. Lauwers, Selective laser melting of iron-based powder, Journal of Materials Processing Technology 149(1) (2004) 616-622.

[76] J. Fuh, Y. Choo, A. Nee, L. Lu, K. Lee, Improvement of the UV curing process for the laser lithography technique, Materials & Design 16(1) (1995) 23-32.

[77] R. Morgan, C. Sutcliffe, W. O'neill, Density analysis of direct metal laser re-melted 316L stainless steel cubic primitives, Journal of materials science 39 (2004) 1195-1205.

[78] M. Rombouts, J.-P. Kruth, L. Froyen, P. Mercelis, Fundamentals of selective laser melting of alloyed steel powders, CIRP annals 55(1) (2006) 187-192.

[79] F. Xiong, Z. Gan, J. Chen, Y. Lian, Evaluate the effect of melt pool convection on grain structure of IN625 in laser melting process using experimentally validated process-structure modeling, Journal of Materials Processing Technology 303 (2022) 117538.

[80] P. Pou-Álvarez, A. Riveiro, X.R. Nóvoa, M. Fernández-Arias, J. del Val, R. Comesaña, M. Boutinguiza, F. Lusquiños, J. Pou, Nanosecond, picosecond and femtosecond laser surface treatment of magnesium alloy: role of pulse length, Surface

and Coatings Technology 427 (2021) 127802.

[81] D. Zhemchuzhnikova, J. Zollinger, Microstructure formation in 6061 aluminum alloy during nano-second pulsed laser processing, Journal of Materials Processing Technology 314 (2023) 117898.

[82] B. Mondal, M. Gao, T.A. Palmer, T. DebRoy, Solidification cracking of a nickel alloy during high-power keyhole mode laser welding, Journal of Materials Processing Technology 305 (2022) 117576.